J. Fluid Mech. (2012), *vol.* 710, *pp.* 505–544.
doi:10.1017/jfm.2012.375

Non-modal stability in sliding Couette flow

R. Liu† and Q. S. Liu†

Key Laboratory of Microgravity (National Microgravity Laboratory), Institute of Mechanics, Chinese Academy of Sciences, Beijing 100190, China

(Received 29 August 2011; revised 9 July 2012; accepted 21 July 2012;
first published online 31 August 2012)

The problem of an incompressible flow between two coaxial cylinders with radii a and b subjected to a sliding motion of the inner cylinder in the axial direction is considered. The energy stability and the non-modal stability have been investigated for both axisymmetric and non-axisymmetric disturbances. For the non-modal stability, we focus on two problems: response to external excitations and response to initial conditions. The former is studied by examining the ϵ-pseudospectrum, and the latter by examining the energy growth function $G(t)$. Unlike the results of the modal analysis in which the stability of sliding Couette flow is determined by axisymmetric disturbances, the energy analysis shows that a non-axisymmetric disturbance has a critical energy Reynolds number for all radius ratios $\eta = a/b$. The results for non-modal stability show that rather large transient growth occurs over a wide range of azimuthal wavenumber n and streamwise wavenumber α, even though the Reynolds number is far below its critical value. For the problem of response to external excitations, the response is sensitive to low-frequency external excitations. For all values of the radius ratio, the maximum response is achieved by non-axisymmetric and streamwise-independent disturbances when the frequency of external forcing $\omega = 0$. For the problem of response to initial conditions, the optimal disturbance is in the form of helical streaks at low Reynolds numbers. With the increase of Re, the optimal disturbance becomes very close to straight streaks. For each η, the maximum energy growth of streamwise-independent disturbances is of the order of Re^2, and the optimal time is of the order of Re. This relation is qualitatively similar to that for plane Couette flow, plane Poiseuille flow and pipe Poiseuille flow. Direct numerical simulations are applied to investigate the transition of the streamwise vortex (SV) scenario at $Re = 1000$ and 1500 for various η. The initial disturbances are the optimal streamwise vortices predicted by the non-modal analysis. We studied the streak breakdown phase of the SV scenarios by examining the instability of streaks. Moreover, we have investigated the sustainment of the energy of disturbances in the SV scenario.

Key words: channel flow, transition to turbulence

1. Introduction

The onset of turbulent fluid motion in a plane channel or a pipe, such as plane Couette flow (PCF), plane Poiseuille flow (PPF) and Hagen–Poiseuille flow (HPF), has received considerable attention over the past few decades. Sliding Couette flow (SCF) is a flow between two co-axial cylinders subjected to a sliding motion of the

† Email addresses for correspondence: liurong@imech.ac.cn, liu@imech.ac.cn

inner cylinder in the axial direction. This type of flow occurs in many industrial applications and medical contexts (Arney *et al.* 1993; Frei, Lüscher & Wintermantel 2000; Walton 2003, 2004, 2005). In comparison with PCF, PPF and HPF, SCF has not been intensively investigated until now, even though the flow has a very simple geometry.

The sliding Couette flow was first investigated by Preziosi & Rosso (1990). However, they did not find any indication of linear instability. Gittler (1993) studied the stability to axisymmetric perturbations for the same problem. The results show that instability occurs for $\eta \leqslant 0.1415$ (where η is the ratio of the cylinder radii a/b) at quite high Reynolds numbers and the linear critical state is absent for $\eta > 0.1415$. Recently, Deguchi & Nagata (2011) have studied the stabilities and bifurcations in SCF. They confirm the linear stability result of Gittler (1993). Moreover, they have extended their analysis to the non-axisymmetric case and found that the stability of the flow is still determined by the axisymmetric perturbations. Their nonlinear analysis shows that finite-amplitude axisymmetric solutions exist far below the critical Reynolds number for $\eta < 0.1415$, and non-axisymmetric travelling wave solutions appear abruptly at a finite Reynolds number regardless of the value of η.

Traditionally, a first step in investigating hydrodynamic stability problems is the normal-mode analysis. For this approach, it is assumed that each mode has an exponential time dependence, thus the base flow is considered to be unstable if an eigenvalue is found in the unstable complex half-plane. The eigenvalue analysis has successfully predicted the instability behaviours for some fluid systems, such as Rayleigh–Bénard convection and Taylor–Couette flow. However, for other instability problems, particularly the instability in shear flows, this approach fails to match most experimental results. For example, eigenvalue analysis shows that plane Couette flow and pipe Poiseuille flow are always stable to infinitesimal disturbances at all Reynolds numbers. However, transition to turbulence is observed for plane Couette flow at Reynolds number $Re \simeq 360$ (Tillmark & Alfredsson 1992) or 370 (Malerud, Måløy & Goldburg 1995), and for pipe Poiseuille flow at $Re \simeq 2000$ (Wygnanski & Champagne 1973; Wygnanski, Sokolov & Friedman 1975). Experiments show that the route to turbulence is highly dependent on the initial conditions and on the continuous forcing that background noise can provide. Such discrepancies between the modal analysis and experiments have been recognized by some authors, and the limiting nature of the eigenvalue approach has led to the emergence of novel ways to investigate the transition from laminar flow to turbulence. In the last few decades two different modelling approaches for transition to turbulence have been proposed. The first one is the non-modal theory which is based on the algebraic transient growth exhibited by the optimal perturbations. The second approach seeks nonlinear wave solutions of the Navier–Stokes equations, by using the concept of self-sustaining processes, and continuation methods.

In the normal-mode analysis, the instability behaviour is inferred from the spectrum of the governing linear operator. Linear systems governed by a normal operator, such as Rayleigh–Bénard convection and Taylor–Couette flow, have orthogonal eigenfunctions. For these normal systems, the spectrum is sufficient to determine the stability of perturbations. However, for a non-normal system the spectrum only describes the asymptotic fate of the perturbations and fails to capture short-term characteristics. The main point of departure of the non-modal theory from the traditional eigenvalue analysis is the fact that even if all of the eigenvalues of a linear system are distinct and lie well inside the stable half-plane, inputs to that system may be amplified by substantially large factors if the linear operator is non-normal. In the non-modal theory, stability is redefined in a broader sense as

the response behaviour of the governing equations to general input variables in the form of initial conditions, external forcing and internal uncertainties. Trefethen *et al.* (1993) addressed the general concept of the non-modal stability theory and studied the transient energy growth and response to external excitations for plane Poiseuille flow and plane Couette flow. Reddy & Henningson (1993) have studied the energy growth in viscous channel flows. The results show that there can be a substantial transient growth in the energy of small perturbations to plane Poiseuille and Couette flows at Reynolds numbers far below the critical value. Schmid & Henningson (1994) have studied the transient energy growth in Hagen–Poiseuille flow. It was found that maximum amplification of initial energy density is realized by disturbances with no streamwise dependence and azimuthal wavenumber $n = 1$. The concept of transient growth has frequently been applied to various hydrodynamic stability problems. For more information on the non-modal stability of hydrodynamic problems, we refer the readers to the review article by Schmid (2007) and the references therein. For more on the mathematics of the behaviour of non-normal linear operators, we refer the readers to the book by Trefethen & Embree (2005).

Given the apparently potent linear amplification of the optimal disturbances predicted by non-modal theory, interest was naturally focused on examining how energy could be fed back from the streaks into the secularly decaying rolls so that the process could be sustainable and thereby accomplish transition. Waleffe (1997) proposed the 'self-sustaining process' (SSP) to understand how turbulence is maintained rather than initiated at low Reynolds numbers. As is well known, the SSP consists of three distinct phases: formation of streamwise streaky flow by streamwise vortices, instability of streaky flow and the regeneration of the streamwise vortices. During streak breakdown, a set of nonlinear interactions re-energizes the streamwise vortices, leading to formation of a new set of streaks, and completing the regeneration cycle. Hamilton, Kim & Waleffe (1995) performed a direct numerical simulation of the cycle for this process consisting of streak formation, breakdown of streaks and regeneration of the streamwise vortices. Reddy *et al.* (1998) studied streak instability in plane channel flow establishing the generic nature of the process. They also performed a direct numerical simulation to investigate the mechanisms of transition for the streamwise vortex (SV) and oblique wave (OW) scenarios. The results showed that streak instability is a fundamental phase of transition initiated by SV and OW scenarios.

A recent new direction in investigating the transition of many wall-bounded shear flows focuses on seeking alternative nonlinear solutions to the Navier–Stokes equations. Coherent solutions, generally unstable and in the form of steady states or travelling waves, have been found for plane channel flow by using homotopy from Taylor–Couette flow (Nagata 1990; Faisst & Eckhardt 2000). The physical mechanism responsible for the coherent structures consists of a three-dimensional, nonlinear self-sustaining process. Following the ideas behind the SSP, Faisst & Eckhardt (2003) and Wedin & Kerswell (2004) have identified some unstable travelling wave solutions for pipe flow.

Stability problems of classical shear flows, such as PCF, PPF and HPF, have been intensively studied using the non-modal theory. However, a careful look at previous work indicates that studies on the stability of SCF have been mostly limited to the framework of classical modal analysis. Until now, the non-modal stability in SCF has attracted much less attention. To the best of our knowledge, the studies on the transient mechanism of SCF are very limited. In addition to the basic wish to understand the stability of SCF, a further reason for the interest is that the narrow-gap limit of SCF

recovers plane Couette flow. One aim of the present paper is to present analogous results for PCF.

In the present work, we aim to study the non-modal stability and transition in SCF, to provide physical insights into the transition from laminar flow towards turbulence. In the non-modal analysis, two types of problems are of particular interest, i.e. response to external excitations and the transient energy growth of initial conditions. We should note that the non-modal analysis in the present paper is based only on a linear local analysis, whereas it is recognized today that the non-modal global approach and nonlinear analysis are important for understanding the transition process (Chomaz 2005). Recently, Cherubini *et al.* (2010) studied the three-dimensional global optimal dynamics of a boundary layer flow by means of an adjoint-based optimization strategy.

After obtaining the optimal disturbances by non-modal theory, we present one scenario in which transition is initiated by optimal streamwise vortices in SCF. Schematically:

(SV) streamwise vortices $\Longrightarrow$ streamwise streaks $\Longrightarrow$ streak breakdown $\Longrightarrow$ transition.

This scenario has been shown to be pertinent in parallel shear flows, such as boundary layers (Schmid & Henningson 2001), plane Couette and plane Poiseuille flows (Reddy *et al.* 1998). The optimal perturbations in the form of two-dimensional streamwise rolls evolve into streamwise streaks via the lift-up mechanism. The amplification of the optimal disturbances can be sufficiently large that the result is the modification of the basic flow rendering it unstable to three-dimensional perturbations. This secondary instability, also referred to as streak breakdown, leads to turbulence. In the present paper, we investigate the streak breakdown phase of the SV scenario via a direct numerical simulation. The breakdown of streaks is necessary but not sufficient for transition to occur. We also studied the sustaining of optimal disturbances in the SV scenario. We should note that the transient growth mechanism is only a possible path in the transition scenario. Recently, some other possible paths of transition have been revisited for typical shear flows. Bottaro, Corbett & Luchini (2003) studied the effect of base flow variation on the stability of plane Couette flow and showed that relatively small changes in the base flow are destabilizing, although the linear base flow in PCF is unconditionally stable.

The remainder of the present paper is organized as follows. In § 2 , the mathematical formulation of the physical model is presented. In § 3, the numerical method for the linear stability problem is presented. In §§ 4 and 5, we present the results and discussions on the energy stability and non-modal stability problem. In § 6, we present the results of direct numerical simulation of the nonlinear evolution for the SV scenario. Finally, we summarize the results and present the conclusions in § 7.

2. Mathematical formulation

Figure 1 illustrates the physical model of the present study. Consider an incompressible flow between two infinitely long concentric cylinders with radii a and b $(b > a)$. The inner cylinder is pulled with an constant speed U in the axial direction while the outer cylinder is kept at rest. The equations governing the evolution of fluid flow are the Navier–Stokes equations expressed as

$$\boldsymbol{\nabla} \cdot \boldsymbol{v} = 0, \tag{2.1}$$

$$\frac{\partial \boldsymbol{v}}{\partial t} + \boldsymbol{v} \cdot \boldsymbol{\nabla} \boldsymbol{v} = -\frac{1}{\rho} \boldsymbol{\nabla} p + \mu \nabla^2 \boldsymbol{v}. \tag{2.2}$$

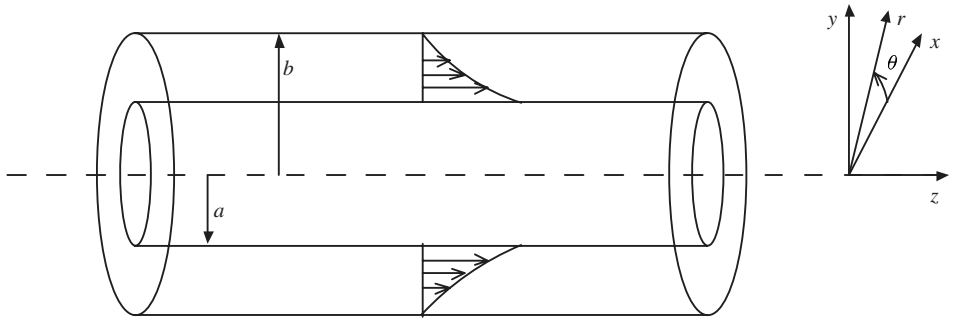

FIGURE 1. Sketch of the geometry of sliding Couette flow. (x, y, z) is a Cartesian coordinate system with z the axial coordinate along the cylinder. A cylindrical coordinate system (r, θ) is chosen at the cylinder centreline $r = 0$.

The boundary conditions on the inner and outer cylinders at $r = a$ and b are

$$u|_{r=a} = v|_{r=a} = 0, \quad w|_{r=a} = U, \quad u|_{r=b} = v|_{r=b} = w|_{r=b} = 0. \tag{2.3}$$

Here ρ is the density, p is the pressure, $\boldsymbol{v} = u\boldsymbol{e}_r + v\boldsymbol{e}_\theta + w\boldsymbol{e}_z$ is the velocity vector, in which u, v and w denote the radial, azimuthal and axial components of the velocity. To non-dimensionalize the problem, we choose the scales of length, time, velocity and pressure as $(b-a)/2$, $(b-a)/2U$, U and ρU^2. The velocity of the base flow can be expressed as

$$\bar{w}(r) = \frac{\ln r(1-\eta)/2}{\ln \eta}. \tag{2.4}$$

Our starting point for the analysis of infinitesimal disturbances in sliding Couette flow is the linearized Navier–Stokes equations. The controlling equations in cylindrical coordinates are expressed as

$$\frac{\partial u'}{\partial r} + \frac{u'}{r} + \frac{1}{r}\frac{\partial v'}{\partial \theta} + \frac{\partial w'}{\partial z} = 0, \tag{2.5}$$

$$\frac{\partial u'}{\partial t} + \bar{w}\frac{\partial u'}{\partial z} = -\frac{\partial p'}{\partial r} + \frac{1}{Re}\left[\Delta u' - \frac{u'}{r^2} - \frac{2}{r^2}\frac{\partial v'}{\partial \theta}\right], \tag{2.6}$$

$$\frac{\partial v'}{\partial t} + \bar{w}\frac{\partial v'}{\partial z} = -\frac{1}{r}\frac{\partial p'}{\partial \theta} + \frac{1}{Re}\left[\Delta v' - \frac{v'}{r^2} + \frac{2}{r^2}\frac{\partial u'}{\partial \theta}\right], \tag{2.7}$$

$$\frac{\partial w'}{\partial t} + \frac{\mathrm{d}\bar{w}}{\mathrm{d}r}u' + \bar{w}\frac{\partial w'}{\partial z} = -\frac{\partial p'}{\partial z} + \frac{1}{Re}\Delta w', \tag{2.8}$$

in which u', v', w' denote non-dimensional disturbance velocity components, and p' denotes non-dimensional pressure disturbance. The boundary conditions on the inner and outer cylinders at $r_i = 2\eta/(1-\eta)$, and $r_o = 2/(1-\eta)$ are

$$u' = v' = w' = 0. \tag{2.9}$$

We expand u', v', w' and p' as superpositions of complex Fourier modes of the form

$$[u', v', w'](r, \theta, z, t) = [\hat{u}, \hat{v}, \hat{w}](r, t)\mathrm{e}^{\mathrm{i}(n\theta + \alpha z)}, \quad p'(r, \theta, z, t) = \hat{p}(r, t)\mathrm{e}^{\mathrm{i}(n\theta + \alpha z)}, \tag{2.10}$$

in which α is the streamwise wavenumber and n is the azimuthal wavenumber, and the hats denotes the Fourier amplitudes of disturbances. The presence of two

homogeneous directions allows us to further reduce the equations to the more convenient radial velocity ($\hat{u}$)–radial vorticity ($\hat{\eta}$) form as suggested by Burridge & Drazin (1969):

$$\left(\frac{\partial}{\partial t}+\mathrm{i}\alpha\bar{w}\right)\mathscr{T}\hat{\Phi}=\mathrm{i}\alpha rk^2\frac{\partial}{\partial r}\left(\frac{1}{rk^2}\frac{\mathrm{d}\bar{w}}{\mathrm{d}r}\right)\hat{\Phi}+\frac{1}{Re}\mathscr{T}\mathscr{T}\hat{\Phi}-\frac{2\alpha n}{Re}\mathscr{T}\hat{\Omega}, \tag{2.11}$$

$$\left(\frac{\partial}{\partial t}+\mathrm{i}\alpha\bar{w}\right)\hat{\Omega}=\frac{\mathrm{i}n}{k^2r^3}\frac{\mathrm{d}\bar{w}}{\mathrm{d}r}\hat{\Phi}+\frac{2\alpha n}{Re}\frac{1}{k^4r^4}\mathscr{T}\hat{\Phi}+\frac{1}{Re}\mathscr{S}\hat{\Omega}, \tag{2.12}$$

in which

$$k^2=\alpha^2+\frac{n^2}{r^2}, \tag{2.13}$$

$$\hat{\Phi}=-\mathrm{i}r\hat{u},\quad \hat{\Omega}=-\frac{\hat{\eta}}{\mathrm{i}k^2r}=\frac{\alpha r\hat{v}-n\hat{w}}{k^2r^2}. \tag{2.14}$$

The operators $\mathscr{T}$ and $\mathscr{S}$ are

$$\mathscr{T}=k^2r\frac{\partial}{\partial r}\left(\frac{1}{k^2r}\frac{\partial}{\partial r}\right)-k^2, \tag{2.15}$$

$$\mathscr{S}=\frac{1}{k^2r^3}\frac{\partial}{\partial r}\left(k^2r^3\frac{\partial}{\partial r}\right)-k^2. \tag{2.16}$$

The original variables can be recovered from

$$\hat{u}=\frac{\mathrm{i}\hat{\Phi}}{r},\quad \hat{v}=-\frac{n}{k^2r^2}\frac{\partial}{\partial r}\hat{\Phi}+\alpha r\hat{\Omega},\quad \hat{w}=-\frac{\alpha}{k^2r}\frac{\partial}{\partial r}\hat{\Phi}-n\hat{\Omega}. \tag{2.17}$$

At $r=r_i, r_o$, the boundary condition are given by the no-slip assumption and can be written in the form

$$\hat{\Phi}=\frac{\partial}{\partial r}\hat{\Phi}=\hat{\Omega}=0. \tag{2.18}$$

The Orr–Sommerfeld equation and the Squire equation can be expressed in vector form as

$$\mathscr{B}\frac{\partial}{\partial t}\boldsymbol{q}=\mathscr{A}\boldsymbol{q}, \tag{2.19}$$

in which $\boldsymbol{q}=(\hat{\Phi},\hat{\Omega})^{\mathrm{T}}$, and the matrices $\mathscr{A}$, $\mathscr{B}$ are

$$\mathscr{B}=\begin{bmatrix}\mathscr{T} & 0\\ 0 & 1\end{bmatrix},\quad \mathscr{A}=\begin{bmatrix}\mathscr{L}_{OS} & \mathscr{L}_d\\ \mathscr{L}_c & \mathscr{L}_{Sq}\end{bmatrix}. \tag{2.20}$$

The operators $\mathscr{L}_{OS}$, $\mathscr{L}_{Sq}$, $\mathscr{L}_c$ and $\mathscr{L}_d$ can be written as

$$\mathscr{L}_{OS}=-\mathrm{i}\alpha\bar{w}\mathscr{T}+\mathrm{i}\alpha rk^2\frac{\partial}{\partial r}\left(\frac{1}{rk^2}\frac{\mathrm{d}\bar{w}}{\mathrm{d}r}\right)+\frac{1}{Re}\mathscr{T}\mathscr{T}, \tag{2.21}$$

$$\mathscr{L}_{Sq}=-\mathrm{i}\alpha\bar{w}+\frac{1}{Re}\mathscr{S}, \tag{2.22}$$

$$\mathscr{L}_c=\frac{in}{k^2r^3}\frac{\mathrm{d}\bar{w}}{\mathrm{d}r}+\frac{2\alpha n}{Re}\frac{1}{k^4r^4}\mathscr{T}, \tag{2.23}$$

$$\mathscr{L}_d=-\frac{2\alpha n}{Re}\mathscr{T}. \tag{2.24}$$

finally, we obtain the linear initial value problem

$$\frac{\partial}{\partial t}\boldsymbol{q} = -\mathrm{i}\mathscr{L}\boldsymbol{q}, \tag{2.25}$$

in which $\mathscr{L} = \mathrm{i}\mathscr{B}^{-1}\mathscr{A}$.

3. Numerical method

In the present paper, we will examine the non-modal stability, including response to external excitations and initial conditions. We need to compute the eigenvalues and eigenvectors of the operator $\mathscr{L}$, the pseudospectrum, the numerical range, and the energy growth function $G(t)$. The spectral method can yield great accuracy for hydrodynamic instability problems. We use a Chebyshev-collocation method to solve the eigenvalue problem, and an eigenmode expansion method to solve the non-modal problem.

We begin with the computation of eigenvalues and eigenvectors. We first transform the $[r_i, r_o]$ domain to the Chebyshev domain $[-1, 1]$ by introducing

$$\zeta = \frac{2(r - r_i)}{r_o - r_i} - 1. \tag{3.1}$$

A Chebyshev collocation method is implemented to solve the eigenvalue problem. The variables $\hat{\Phi}$ and $\hat{\Omega}$ are expanded as

$$\hat{\Phi} = \sum_{n=0}^{N} a_n T_n(\zeta), \quad \hat{\Omega} = \sum_{n=0}^{N} b_n T_n(\zeta), \tag{3.2}$$

in which T_n denotes the nth Chebyshev polynomial.

Using the Chebyshev series (3.2) and substituting $\partial/\partial t$ with $-\mathrm{i}\omega$, the governing equations and the no-slip boundary conditions can be written in discrete form

$$\mathscr{A}\boldsymbol{x} = \omega\mathscr{B}\boldsymbol{x}, \tag{3.3}$$

in which $\boldsymbol{x} = [a_0, \ldots, a_N, b_0, \ldots, b_N]^{\mathrm{T}}$, and $\mathscr{A}, \mathscr{B}$ arise from discretization of the controlling equations and boundary conditions.

This system of equations is required to solve for $2N + 2$ unknowns. The numerical method for general eigenvalue problems in the form $\mathscr{A}\boldsymbol{x} = \omega\mathscr{B}\boldsymbol{x}$ has been described by Canuto *et al.* (1993) and Schmid & Henningson (2001). The Orr–Sommerfeld-like equation, (2.11), is fourth-order, so the equation is applied at $N - 3$ internal collocation points and at each boundary the equations are replaced by two boundary conditions. The Squire-like equation (2.12) is second-order, and it is applied at $N - 1$ internal collocation points with only one boundary condition applied at each boundary. The details of imposing boundary conditions in the collocation method are described by Canuto *et al.* (1993).

We have solved the eigenvalue problem for different values of n and α at a wide range of Reynolds numbers. The convergence and reliability of the code have been checked. Some of the results reported here are compared with previous work in table 1. After we solve the eigenvalue problem, an eigenmode expansion method can be used to compute the transient energy growth and the response to external excitations. The computational method is a standard procedure, and we refer the readers to the works by Reddy & Henningson (1993) and Schmid & Henningson (1994).

In non-modal stability theory, stability is redefined in a broader sense as the response to general input variables, including initial conditions, impulsive and

	(n, α)	η	Re	N	ω_r	ω_i
Present work	(3, 3)	1/3	1000	50	0.19232143	−0.12378071
Present work	(3, 3)	1/3	1000	100	0.19232143	−0.12378071
Preziosi & Rosso (1990)	(3, 3)	1/3	1000	30	0.1923	−0.1238
Present work	(0, 0.6546)	0.1	3.6×10^6	150	0.62980689	−0.00000201
Present work	(0, 0.6546)	0.1	3.6×10^6	240	0.62980687	−0.00000201
Deguchi & Nagata (2011)	(0, 0.6546)	0.1	3.6×10^6	140	0.62980833	−0.00000202
Present work	(1, 2.0)	0.01	4×10^7	550	0.00432150	−0.00117465
Present work	(1, 2.0)	0.01	4×10^7	600	0.00432150	−0.00117465
Deguchi & Nagata (2011)	(1, 2.0)	0.01	4×10^7	600	0.00432150	−0.00116964

TABLE 1. Leading eigenvalues for several typical cases.

continuous external excitations. Like most previous work on the subject of non-modal analysis on hydrodynamic stabilities, we are interested in responses to continuous external excitations and initial conditions.

Now we begin with the responses to external excitations. Suppose a fluid system is driven by a signal of the form

$$\boldsymbol{q}_{in}(x, y, z, t) = \exp(-\mathrm{i}\omega t)\boldsymbol{Q}_{in}(x, y, z), \tag{3.4}$$

in which ω is the complex frequency. Then the response $\boldsymbol{q}_{out}(x, y, z, t)$ and the input signal $\boldsymbol{q}_{in}(x, y, z, t)$ satisfy the equation

$$\frac{\partial}{\partial t}\boldsymbol{q}_{out} = -\mathrm{i}\mathscr{L}\boldsymbol{q}_{out} + \exp(-\mathrm{i}\omega t)\boldsymbol{Q}_{in}. \tag{3.5}$$

From (3.5), we obtain the response $\boldsymbol{q}_{out}$ in the form of

$$\boldsymbol{q}_{out}(x, y, z, t) = \mathrm{i}\,(\omega\mathscr{I} - \mathscr{L})^{-1}\,\boldsymbol{q}_{in}(x, y, z). \tag{3.6}$$

Here $\mathscr{I}$ is the identity matrix. The solution operator $(\omega\mathscr{I} - \mathscr{L})^{-1}$ is known as the resolvent. We denote the maximum amplification of a disturbance at frequency ω by $\mathscr{R}(\omega)$. $\mathscr{R}(\omega)$ is equal to the norm of the resolvent and expressed as

$$\mathscr{R}(\omega) = \sup_{\boldsymbol{q}_{in}\neq 0} \frac{\|\boldsymbol{q}_{out}\|}{\|\boldsymbol{q}_{in}\|} = \|\,(\omega\mathscr{I} - \mathscr{L})^{-1}\,\|. \tag{3.7}$$

Here $\|\cdot\|$ denotes a norm on $\mathbb{C}^N$, 'sup' denotes the maximum. An eigenvalue of $\mathscr{L}$ is a number ω such that $\|\,(\omega\mathscr{I} - \mathscr{L})^{-1}\,\| \to \infty$. Generalizing this result leads naturally to the definition of the 'ϵ-pseudospectrum' (Trefethen & Embree 2005). For any $\epsilon \geqslant 0$, the ϵ-pseudospectrum of $\mathscr{L}$ is defined as

$$\Lambda_\epsilon(\mathscr{L}) = \{\omega \in \mathbb{C} : \|\,(\omega\mathscr{I} - \mathscr{L})^{-1}\,\| \geqslant \epsilon^{-1}\}. \tag{3.8}$$

The quest for maximum amplification of initial conditions is of particular interest in many hydrodynamic stability problems. For the linear system (2.25), the solution has the form

$$\boldsymbol{q}(t) = \exp(-\mathrm{i}\mathscr{L}t)\boldsymbol{q}(0). \tag{3.9}$$

The maximum amplification of the initial condition can be described by the growth function $G(t)$ as

$$G(t) = \max_{\boldsymbol{q}(0)\neq 0} \frac{\|\boldsymbol{q}(t)\|^2}{\|\boldsymbol{q}(0)\|^2} = \|\mathrm{e}^{-\mathrm{i}\mathscr{L}t}\|^2 . \tag{3.10}$$

We should note that $\mathscr{R}(\omega)$ and $G(t)$ are related to the choice of definition of the norm $\|\cdot\|$. In the present paper, we choose the norm $\|\cdot\|$ as the energy norm. For variable $\boldsymbol{q}$, we will make use of a scalar product based on energy density defined as

$$(\boldsymbol{q}_1, \boldsymbol{q}_2)_{\mathscr{M}} = \pi \int_{r_i}^{r_o} r \left[\frac{\mathrm{D}\hat{\Phi}_1 \mathrm{D}\hat{\Phi}_2^*}{k^2 r^2} + \frac{\hat{\Phi}_1 \hat{\Phi}_2^*}{r^2} + k^2 r^2 \hat{\Omega}_1 \hat{\Omega}_2^* \right] \mathrm{d}r, \tag{3.11}$$

in which $*$ denotes the complex conjugate. Based on this scalar product, the associated energy norm is given as follows:

$$\|\boldsymbol{q}\|^2_{\mathscr{M}} = (\boldsymbol{q}, \boldsymbol{q})_{\mathscr{M}} = \pi \int_{r_i}^{r_o} r[|\hat{u}|^2 + |\hat{v}|^2 + |\hat{w}|^2] \, \mathrm{d}r. \tag{3.12}$$

The computation of response to external forcing and the energy growth function can be accomplished using an eigenvector expansion method; see Reddy & Henningson (1993) and Schmid & Henningson (1994) for details of the procedure.

4. Condition for no energy growth

In this section, we are interested in the condition for which there is no growth of the perturbation kinetic energy. Energy methods give conditions for no energy growth. From (2.25) we have:

$$\frac{\mathrm{d}}{\mathrm{d}t}\mathscr{E} = \frac{\mathrm{d}}{\mathrm{d}t} \|\boldsymbol{q}\|^2_{\mathscr{M}} = 2 \, \mathrm{Im} \, (\mathscr{L}\boldsymbol{q}, \boldsymbol{q})_{\mathscr{M}}, \tag{4.1}$$

in which $\mathscr{E}$ is the kinematic energy. There is no energy growth if and only if all the eigenvalues of the antisymmetric parts of $\mathscr{L}$, $(\mathscr{L} - \mathscr{L}^H)/2$, lie in the lower half-plane. The energy method shows that there is no energy growth if the Reynolds number is less than a certain value. We denote this critical energy Reynolds number by Re_1. In order to determine its value, two methods can be used: compute the eigenvalues of $(\mathscr{L} - \mathscr{L}^H)/2$, or solve the optimization problem using a variational method. Reddy & Henningson (1993) used the variational method to study the energy stability of plane Couette and Poiseuille flow. Joseph & Munson (1970) and Hung, Joseph & Munson (1972) studied the energy stability of spiral flow between rotating and sliding cylinders. For hydrodynamics stability problems, the linear stability theory gives the sufficient conditions for instability, and the energy theory gives the sufficient conditions for stability.

We now examine the condition below which the kinetic energy of an infinitesimal disturbance decays monotonically. Let σ be the leading eigenvalue of $(\mathscr{L} - \mathscr{L}^H)/2$. The initial energy growth is determined by $\sigma(n, \alpha, \eta, Re)$. For a fixed radius ratio η, the condition with no energy growth is given by the energy Reynolds number Re such that $\sigma = 0$. For a given η, the global critical energy Reynolds number is given by $Re_{crit} = \min_{n,\alpha} Re(n, \alpha)$, in which $\sigma(n, \alpha, \eta, Re) = 0$.

Figure 2 presents the critical energy Reynolds number versus the wavenumber for various azimuthal wavenumbers at some typical values of the radius ratios. Figure 2(*a*) displays the curves of the energy Reynolds number for $\eta = 0.01$, which is close to

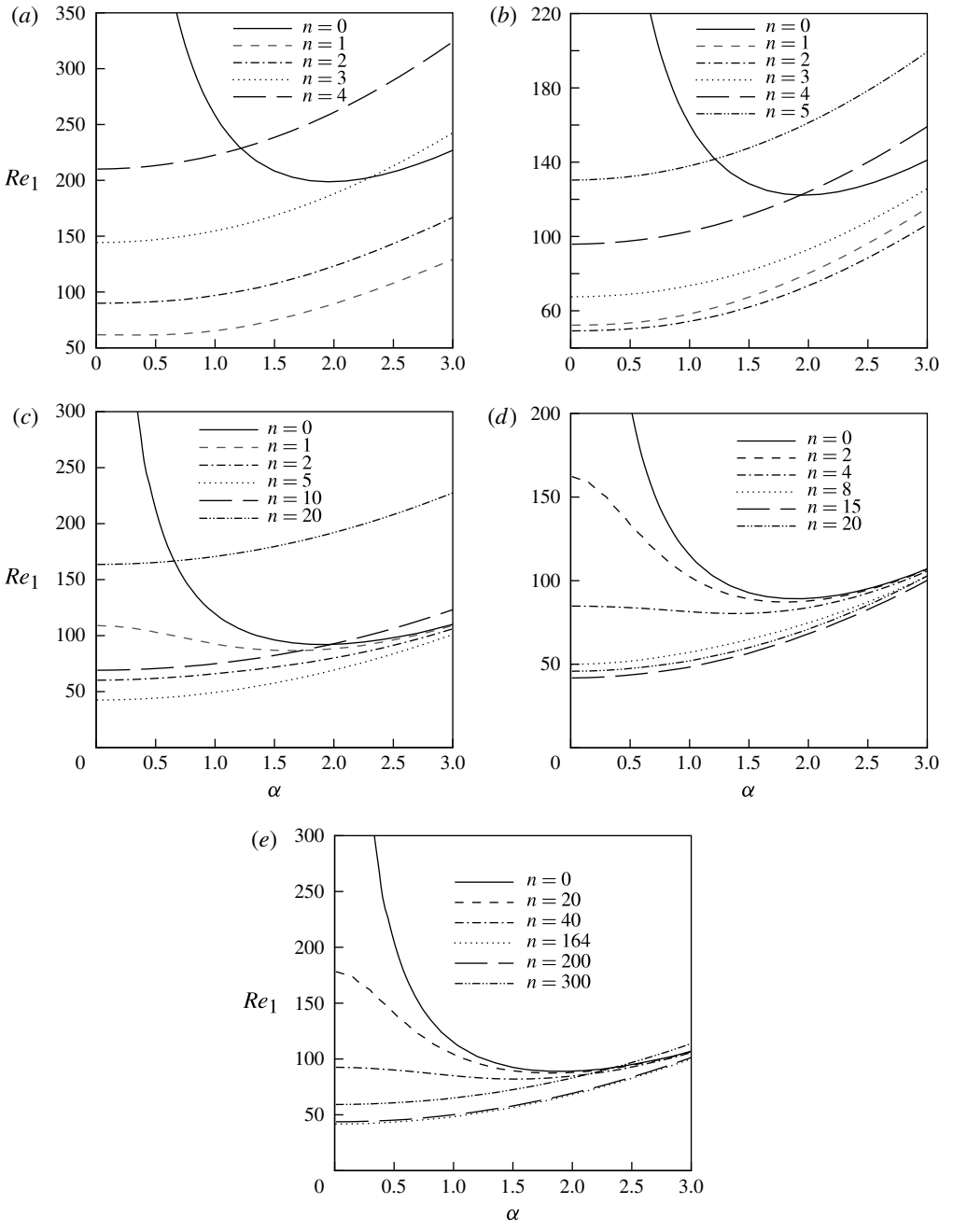

FIGURE 2. Critical energy Reynolds number versus the streamwise wavenumber for various η. (*a*) $\eta = 0.01$; (*b*) $\eta = 0.1$; (*c*) $\eta = 0.5$; (*d*) $\eta = 0.8$; (*e*) $\eta = 0.98$.

the wide-gap limit of $\eta \to 0$. In this figure, it is shown that for the axisymmetric case of $n = 0$, the minimal critical energy Reynolds number is $\sim$200 at $\alpha \simeq 2.0$. The critical energy Reynolds number for $n = 1$ is much lower than that of the axisymmetric case of $n = 0$ at all streamwise wavenumbers. The structures of the curves of $n \geqslant 1$

are similar and the minimal critical value is always realized at the long-wave limit of $\alpha = 0$ and the energy Reynolds number increases with the increase of α. For $n \geqslant 1$, the energy Reynolds number significantly increases with the increase of n at all streamwise wavenumbers. The streamwise-uniform disturbance with $n = 1$ has the lowest critical energy Reynolds number of $Re_1 \simeq 53$ for $\eta = 0.01$.

In figure 2(*b*), the curves of the critical energy Reynolds number are displayed for $\eta = 0.1$. The structures of the curves of the axisymmetric case ($n = 0$) and non-axisymmetric cases ($n \geqslant 1$) are similar to those of $\eta = 0.01$ in figure 2(*a*). However, the lowest critical energy Reynolds number is given by mode $n = 2$ instead of $n = 1$ for $\eta = 0.01$ in figure 2(*a*). For $n \geqslant 2$, the critical value increases with the increase of n at all streamwise wavenumbers.

In figure 2(*c–e*), the curves of narrow-gap cases are displayed for several typical values of $\eta = 0.5$, 0.8 and 0.98. In these figures, the structures of the curves of the axisymmetric case are similar to those of the wide-gap cases in figure 2(*a,b*). For $n = 0$, the minimal critical value of Re decreases with the increase of η in the wide-gap case. An increase in η has almost no influence on the value of the critical energy Reynolds number. As $\eta \to 1$, SCF reduces to the limit case of PCF. For the axisymmetric case of $n = 0$, the critical value of Re_1 for $\eta = 0.98$ is $\sim$88.9 at $\alpha \simeq 1.95$, which is very close to the result for PCF in which $Re_1 \simeq 44.6$ at $\alpha \simeq 1.9$ for spanwise-uniform disturbances (Liu & Liu 2011). (Note that in SCF, the velocity scale is twice that in PCF.) For axisymmetric cases, the two-dimensional Reynolds stress mechanism is responsible for the energy growth of the disturbance with streamwise variations. In these figures the critical energy Reynolds numbers for $n = 0$ tend to infinity as the streamwise is close to zero, because for $\alpha = 0$ there is no streamwise variation of the disturbance. For non-axisymmetric disturbances in the form of streamwise vortices, the lift-up mechanism is responsible for the energy growth of disturbances. In figure 2(*a–e*) for non-axisymmetric cases with $n \neq 0$, the critical energy Reynolds number is finite as α tends to zero due to the lift-up effect. In figure 2(*a,b*), for each value of $n \neq 0$, the streamwise wavenumber of the critical mode with the lowest Re_1 is close to zero. In figure 2(*c–e*) for narrow-gap cases, it is interesting that for some curves with $n \neq 0$, the critical mode is in the form of oblique waves, i.e. disturbances with $n \neq 0$ and $\alpha \neq 0$. For $\eta = 0.5$, 0.8 and 0.98 with $n = 1$, 2 and 20, it is found that the spanwise wavelengths of these modes are much larger than unity. So, for these modes of disturbance the variations in the spanwise direction are small. In these cases, the lift-up effect is weak and the two-dimensional Reynolds stress mechanisms are dominant. Thus, for the modes with long spanwise wavelengths, the critical modes are in the form of oblique waves instead of streamwise vortices.

In figure 2(*c–e*), modes $n = 5$, 15 and 164 have the lowest critical energy Reynolds number, respectively. For $\eta = 0.98$, the lowest critical energy Reynolds number $Re_1 \approx 42$. This value is consistent with that for PCF in which $Re_1 \approx 21$ (Schmid & Henningson 2001). For PCF, it has been shown that the optimal disturbance has a spanwise wavenumber $\beta \simeq 1.6$. We infer that in the narrow-gap case for SCF, the azimuthal wavelength is close to the spanwise wavelength in PCF, i.e. the relation between the azimuthal wavenumber n of the critical mode and the spanwise wavenumber β for PCF is given by $n \simeq \beta(1 + \eta)/(1 - \eta)$. As shown in figure 2(*e*), for $\eta = 0.98$ the azimuthal wavenumber of the critical mode obtained from the numerical method is 164. The estimated value of the spanwise wavelength is 1.657 for SCF, which is very close to $\beta \approx 1.6$ for PCF.

In linear stability analysis, the stability of SCF is determined by axisymmetric perturbations. Only when $\eta \leqslant 0.1415$, can SCF become linearly unstable when the

Reynolds number exceeds the critical value. However, the results of our energy analysis indicate that the condition with no energy growth is determined by non-axisymmetric perturbations for all radius ratios.

5. Transient behaviour and non-modal stability

In the non-modal theory, two types of problems are of particular interest, i.e. response to external excitations and transient energy growth of initial conditions. For the former, the norm of the resolvent denotes the maximum amplification of external excitations; for the latter, the growth function $G(t)$ identifies the optimal growth of energy at time t. For the initial problem, we may be interested in the energy growth rate at the initial stage. The concept of numerical range can be used to link the operator to the initial energy growth. The numerical range is defined as

$$W(\boldsymbol{A}) = \{\boldsymbol{x}^*\boldsymbol{A}\boldsymbol{x} : \boldsymbol{x} \in \mathbb{C}^N, \|\boldsymbol{x}\| = 1\}, \tag{5.1}$$

in which $\boldsymbol{A} \in \mathbb{C}^{N\times N}$. The numerical abscissa of $\boldsymbol{A}$ is defined as:

$$\omega(\boldsymbol{A}) = \sup_{z\in W(\boldsymbol{A})} \mathrm{Re}(z) = \lim_{t\to 0} \frac{\mathrm{d}}{\mathrm{d}t}\|\mathrm{e}^{\boldsymbol{A}t}\|. \tag{5.2}$$

The main application of numerical range is to the analysis of energy growth for initial-value problems. The numerical abscissa of $-\mathrm{i}\mathscr{L}$ corresponds to the initial growth rate of the energy growth function (Reddy & Henningson 1993; Trefethen & Embree 2005).

Before we present the results of the non-modal stability of SCF, it is helpful to examine the mechanisms of perturbation growth and decay. As discussed in previous works, the two-dimensional Reynolds stress mechanism exists in plane shear flows (Pedlosky 1987). We will show that a similar mechanism also exists in SCF. We consider the energy equation for inviscid perturbation:

$$\frac{\partial e}{\partial t} + W\frac{\partial}{\partial z}e = -\frac{1}{r}\frac{\partial}{\partial r}(rup) - \frac{1}{r}\frac{\partial}{\partial \theta}(pv) - \frac{\partial}{\partial z}(pw) - uwW', \tag{5.3}$$

in which $e = (u^2 + v^2 + w^2)/2$, W is the mean axial flow, and the prime denotes $\mathrm{d}/\mathrm{d}r$. Upon volume-integration, the advection and pressure-work terms drop out, yielding

$$\frac{\mathrm{d}}{\mathrm{d}t}\mathscr{E} = -\int uwW'\,\mathrm{d}V. \tag{5.4}$$

This expression indicates that a disturbance can extract energy from the mean shear, and positive Reynolds stress $uw > 0$ is necessary for energy growth. To understand this mechanism, let us consider the axisymmetric perturbation. We define a perturbation streamfunction ψ, with $w = r^{-1}\partial\psi/\partial r$, $u = -r^{-1}\partial\psi/\partial z$. We can distinguish two types of streamlines: 'positive-tilt' streamlines are those tilting towards the mean shear, i.e. positive uw, whereas 'negative-tilt' streamlines are those tilting in the streamwise direction, i.e. negative uw. This mechanism has also been discussed by Orr associated with conservation in a strain field of spanwise perturbation vorticity (Orr 1907), and it will be referred to as the Orr mechanism. Farrel & Ioannou (1993) studied this mechanism in plane shear flows. In the present paper, we have extended this mechanism from plane shear flows to sliding Couette flow.

In addition to the two-dimensional Reynolds stress mechanism, another growth mechanism, i.e. the 'lift-up' effect, plays an important role in the amplification of disturbances in shear flows. In experiments, streamwise streaks, i.e. narrow regions

where the streamwise velocity is larger or smaller than the average, are very commonly observed in plane shear flows (Kline *et al.* 1967; Kitoh, Nakabyashi & Nishimura 2005). These alternating longitudinal high- and low-velocity streaks are independent of the two-dimensional Tollmien–Schlichting (TS) waves. Transition that does not follow the traditional route of exponential instability is known as 'bypass transition' (Schmid & Henningson 2001). The mechanism for the transient growth in shear flows has been noted to be inviscid in nature. It has been shown that, for inviscid shear flows, the streamwise velocity grows linearly with time for disturbances with no streamwise variation (Ellingsen & Palm 1975). This growth mechanism has been labelled lift-up and vortex stretching, or more accurately vortex tilting. As explained by several authors (Butler & Farrell 1992; Trefethen *et al.* 1993), for viscous shear flows the streamwise velocity grows linearly with time via the lift-up effect before being damped by the viscosity. In order to find the growth mechanism of streamwise-uniform streaks in SCF, it is helpful to recall the linearized momentum equation for the streamwise velocity component w of streamwise-uniform disturbances:

$$\frac{\partial}{\partial t}w = -W'u. \tag{5.5}$$

The components u, v of the streaks are independent of time and z, so the streamwise component w increases linearly with time. To understand further the effect of mean shear on the tilting or stretching of vorticity, we consider the inviscid vorticity equation for streamwise-independent disturbances:

$$\frac{\partial \Omega_r}{\partial t} = W'\left(\frac{1}{r}\frac{\partial u}{\partial \theta}\right), \tag{5.6}$$

where Ω_r is the radial vorticity component. Note that $-W'$ is the azimuthal component of the mean vorticity. From this expression, the mean shear generates and amplifies Ω_r whenever u is non-zero. Farrel & Ioannou (1993) studied the optimal excitation of three-dimensional perturbations in viscous plane shear flows, and found that the optimal structures can be interpreted as combinations of two fundamental types of motion associated with the lift-up mechanism and the two-dimensional Reynolds stress mechanism.

5.1. *Pseudospectrum and response to external excitations*

The behaviour of a non-normal operator depends not solely on the eigenvalues (spectrum), but also on the structure of ϵ-*pseudospectra*. As discussed in § 3, the resolvent norm represents the amplification of response to external forcing. In order to find the response to external excitations, we plot the ϵ-pseudospectra for several typical parameters.

In figure 3, we plot the ϵ-pseudospectra and the spectrum for axisymmetric and non-axisymmetric disturbances in a wide-gap case of $\eta = 0.1$ at $Re = 2000$. As shown in figure 3(*a*,*b*) for the disturbances with $\alpha = 1$, the structure of the spectrum consists of three branches. For plane and pipe Poiseuille flow, the eigenvalues are located on three main branches, called A, P and S (Schmid & Henningson 2001). The A modes, which have largest variation close to the wall, have rather small phase velocities, whereas, the P modes, which have their maxima close to the centre of the channel, have much higher phase speeds. The S modes, which are highly damped, have a phase speed that is nearly equal to 2/3. In figure 3, the spectra of sliding Couette flow do not contain a P branch, but have two A branches. The spectrum on the left branch and the right branch are the wall modes related to the outer and inner walls, respectively.

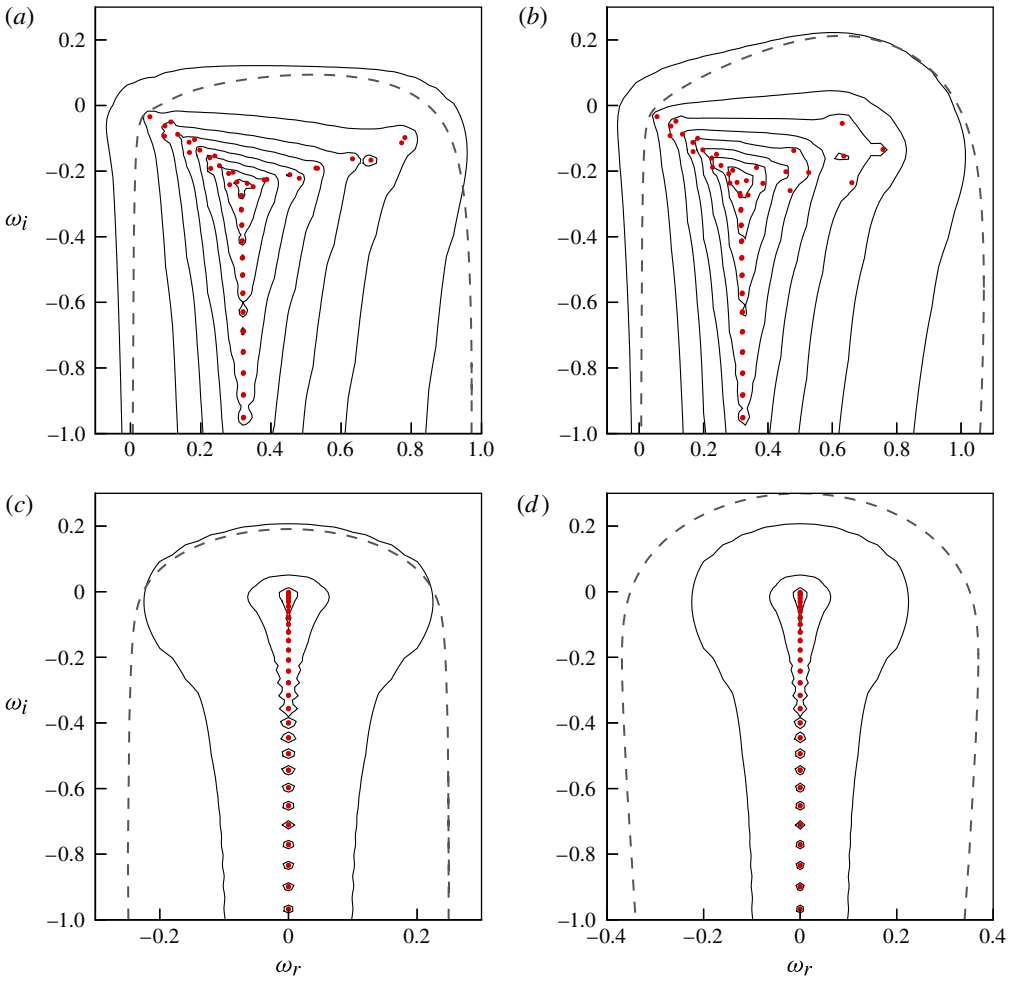

FIGURE 3. (Colour online) Pseudospectra for the sliding Couette flow with $Re = 2000$ and $\eta = 0.1$ for various n. (*a*) $n = 0$, $\alpha = 1.0$; (*b*) $n = 1$, $\alpha = 1.0$; (*c*) $n = 1$, $\alpha = 0$; (*d*) $n = 2$, $\alpha = 0$. ●, Eigenvalues (spectrum); – – –, boundary of the numerical range; —, contours from outermost to innermost (ith) represent levels from $\epsilon = 10^{-1}$ to 10^{-i}.

In figure 3(*a,b*), the intersection region between the A mode and S mode has very small values of ϵ. This means that this region is highly sensitive to disturbances. For $n = 0$ and 1, the numerical abscissa is positive. This means that at the initial time the energy of the disturbance is growing. Comparing figure 3(*a*) with 3(*b*), it is found that the numerical range protrudes deeper into the upper plane for $n = 1$ than for $n = 0$. This result indicates that the energy of non-axisymmetric disturbances grows more rapidly than that of axisymmetric disturbances at the initial stage.

In figure 3(*a*) for the axisymmetric case, the eigenvalues of the inner wall mode are nearly in a straight line. However, in figure 3(*b*) for the non-axisymmetric case, being similar to plane Couette flow, the eigenvalues of both the outer wall mode and the inner wall mode are on three straight lines. Being different from the plane Couette flow, these two A branches are not symmetric about the S branch. Figure 3(*c,d*) show the ϵ-pseudospectrum and spectrum for streamwise-uniform disturbance for $n = 1$

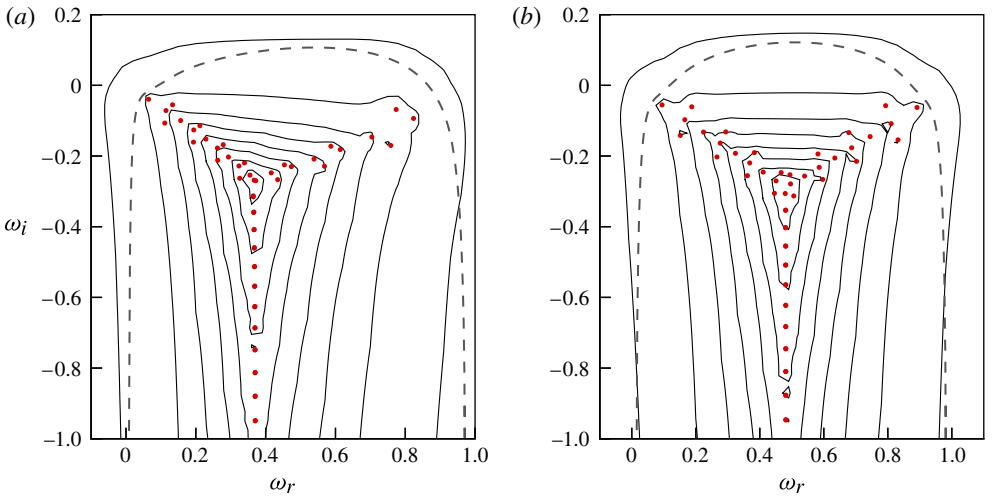

FIGURE 4. (Colour online) Pseudospectra for the sliding Couette flow with $\alpha = 1.0$, $n = 0$ at $Re = 2000$. (*a*) $\eta = 0.2$; (*b*) $\eta = 0.8$. ●, Eigenvalues (spectrum); − − −, boundary of the numerical range; —, contours from outermost to innermost (*i*th) represent levels from $\epsilon = 10^{-1}$ to 10^{-i}.

and 2; the structures of the pseudospectrum and eigenvalues are qualitatively similar to the Squire mode of plane Couette flow.

The radius ratio is an important parameter influencing the stability in SCF. We plot in figure 4 the pseudospectrum and spectrum of a streamwise non-uniform disturbance with $\alpha = 1$, $n = 0$ for $\eta = 0.2$ and 0.8. For $\eta = 0.2$, the structure of the spectrum is similar to that of $n = 1$ and $\eta = 0.1$ in figure 3(*b*). As the ratio increases to 0.8, the two A branches become almost symmetric about the S branch. Increasing the value of η further (not shown), we find that the S branch moves towards the location of $\omega_r = 0.5$ which coincides with the location of the S branch in PCF. We infer that in the narrow-gap case the response behaviour of axisymmetric disturbances in SCF is close to the spanwise-uniform disturbance in PCF. We also computed the spectrum of streamwise-independent cases for various values of η. The structures of the spectrum of $\alpha = 0$ and $n > 0$ are qualitatively similar to figure 3(*c,d*).

In the complex-ω-plane, we are particularly interested in the resonance along the real axis because it corresponds to external excitations at real frequencies. Schmid & Henningson (2001) derived the bounds on the maximum response as

$$\frac{1}{\mathtt{dist}(\Lambda(\mathscr{L}) - \omega)} \leqslant \mathscr{R}(\omega) \leqslant \frac{\mathtt{cond}(\boldsymbol{F})}{\mathtt{dist}(\Lambda(\mathscr{L}) - \omega)} \tag{5.7}$$

where $\mathtt{cond}(\boldsymbol{F})$ is the condition number of the matrix $\boldsymbol{F}$ and $\mathtt{dist}(\Lambda(\mathscr{L}) - \omega)$ is the closest distance between ω and the eigenvalue of $\mathscr{L}$. Here $\boldsymbol{F}\boldsymbol{F}^* = \boldsymbol{M}$, where $\boldsymbol{M}$ is the matrix defined in terms of the inner product

$$M_{i,j} = (\tilde{\boldsymbol{q}}_i, \tilde{\boldsymbol{q}}_j), \tag{5.8}$$

in which $\tilde{\boldsymbol{q}}_i$ and $\tilde{\boldsymbol{q}}_j$ are the *i*th and *j*th eigenvectors. It follows from (5.7) that there are in principle two distinct ways to get a large response: either the forcing frequency ω is close to an eigenvalue of the linear operator or there is a large condition number $\mathtt{cond}(\boldsymbol{F})$ that indicates that the linear operator is highly non-normal. The first case is called 'at resonance'. The second case is called 'off-resonance', i.e. the difference

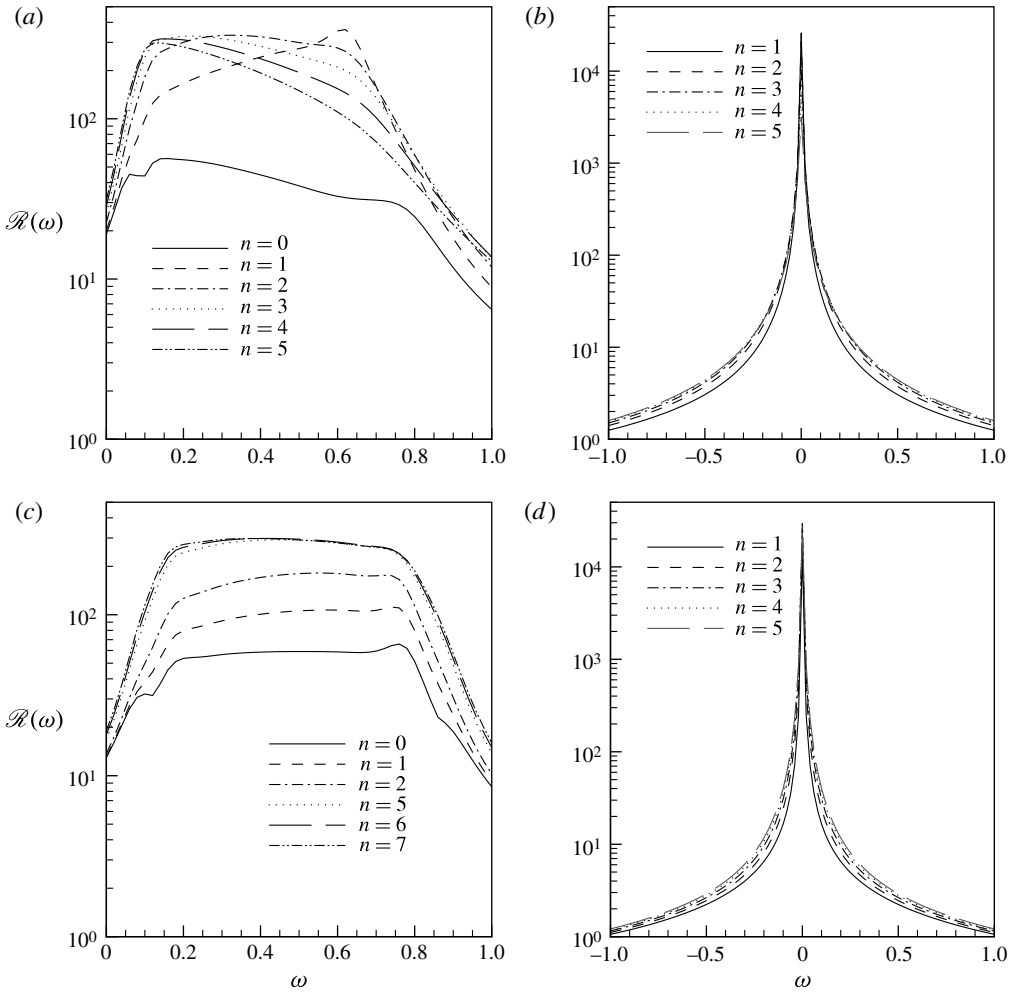

FIGURE 5. The curves of the maximum response $\mathscr{R}(\omega)$ to the harmonic external forcing versus the real frequency ω at $Re = 2000$. (*a*) $\alpha = 1.0$, $\eta = 0.1$; (*b*) $\alpha = 0$, $\eta = 0.1$; (*c*) $\alpha = 1.0$, $\eta = 0.5$; (*d*) $\alpha = 0$, $\eta = 0.5$.

between the forcing frequency and the spectrum can be large, and yet can exhibit a large response (Schmid & Henningson 2001).

In figure 5, we plot the maximum response to spatially harmonic forcing at a wide range of frequencies. As shown in figure 3(*a,b*), the eigenmodes are mainly located on three main branches. The intersection region is very sensitive to disturbances. For $\alpha = 1$ in figure 5(*a,c*), all the curves show that external forcing is significantly amplified in a limited band of frequency. The inner region of the plateau shape is mainly due to the resonance between the intersection region and disturbances (off-resonance), and the boundary region is mainly due to the resonance of the left and right branches (at resonance). As shown in figure 5(*a,c*) for the streamwise-dependent case, the magnitudes of the response due to 'at resonance' and 'off-resonance' are comparable. Outside the plateau region, the points of the real axis in the complex-ω-plane are far from the eigenmode branches, so the resonance is weak.

For the wide-gap case of $\eta = 0.1$ as shown in figure 5(*a*), the axisymmetric external forcing is amplified the least in comparison with other modes. The external forcing of $n = 1$ is amplified the most at a frequency close to the frequency of the inner wall mode. As n increases to 2, the amplification decreases in the right-hand region and increases in the left-hand region. As n increases further, the curves of $n = 2, 3, 4, 5$ show that the amplification gradually decreases in the right-hand region. However, with the increase of n from 2 to 5, the amplification in the left-hand region of the band is insensitive to n. In figure 5(*c*) for $\eta = 0.5$, the curves of amplification become flatter in the limited band than the curves in figure 5(*a*) for $\eta = 0.1$.

For the streamwise-independent case, as shown in figure 3(*c,d*) the spectra are located on the imaginary axis in the stable half-plane. The isolines of ϵ-pseudospectra show that the spectra are sensitive to disturbances. The resonance between the spectra and disturbance results in a substantial response to external forcing in the low-frequency range. With the increase of the frequency of forcing (ω), the resonance becomes weaker because the frequency differences between the eigenmodes and external forcing increase. Figure 5(*c,d*) displays the curves of the maximum amplification of streamwise-independent external forcing for $\eta = 0.1$ and 0.5. The external forcing is amplified most in the low-frequency limit of $\omega = 0$, and the amplification decreases with the increase of the magnitude of ω. Comparing figure 5(*c*) with 5(*a*) and 5(*d*) with5(*b*) shows that the maximum amplification of the streamwise-independent forcing is much higher than that of the streamwise-dependent case. As shown in figure 3, the least stable eigenvalue in the streamwise-independent case is closer to the real axis than in the streamwise-dependent case. So, in the 'at resonance' case, the response in the streamwise-independent case is much higher than in the streamwise-dependent case. This result is qualitatively similar to that for plane Couette flow and Poiseuille flow.

Figure 5 only provides us with the maximum response to a spatially harmonic forcing. In order to obtain the maximum response to stochastic external forcing, we need to examine the global behaviour of the operator $\mathscr{L}$ for continuous streamwise wavenumbers and various azimuthal wavenumbers. In figure 6, the ϵ-pseudospectra and the spectrum of $n = 0$ and $n = 5$ are plotted for $\eta = 0.5$ at $Re = 2000$. For each (α, n) pair, the spectrum is discrete. We fix n and change α; all the eigenvalues of $\mathscr{L}$ are within the shaded region. In figure 6(*a,b*), the spectrum is located in the lower half-plane, and the isolines of $\log\epsilon$ are plotted. Comparing figure 6(*a*) with figure 6(*b*), the isoline with the same value protrudes deeper into the upper plane for $n = 5$ than for $n = 0$. This result means that the non-axisymmetric external forcing of $n = 5$ is amplified by a higher factor than the axisymmetric one. Trefethen *et al.* (1993) have plotted the spectrum of the continuous operator $\mathscr{L}$ for plane Couette flow and Poiseuille flow. The structures of the shaded region in figure 6 are similar to that of plane Couette flow in Trefethen *et al.* (1993). We should remark that for plane shear flows, the spectrum is continuous in the shaded region in the ω-plane. However, for sliding Couette flow, the spectrum of the continuous operator is only restricted in the shaded region instead of fulfilling it. The eigenvalues are located within the shaded region, but they are discrete. In figure 7, the ϵ-pseudospectra and the spectrum of $n = 0$ and $n = 1$ are plotted for a wide-gap case of $\eta = 0.01$ at $Re = 2000$. Comparing figure 7(*a*) with figure 6(*a*), it is found that the shaded region of the spectrum significantly shrinks in the ω-plane with the decrease of η. Comparing figure 7(*b*) with figure 7(*a*), it is also found that the response of the non-axisymmetric external forcing is higher than that of the axisymmetric one.

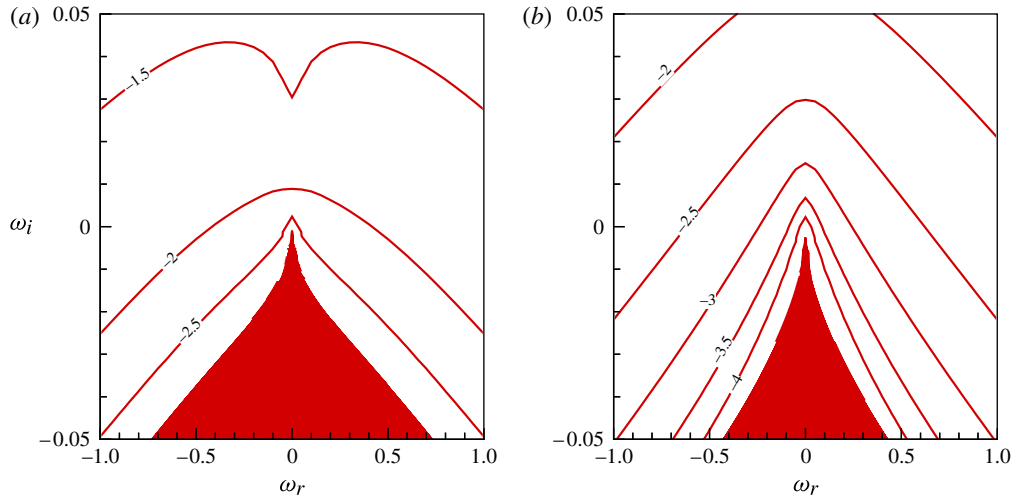

FIGURE 6. (Colour online) Pseudospectra for sliding Couette flow at $Re = 2000$, $\eta = 0.5$. (a) $n = 0$; (b) $n = 5$. The contours represent the level of $\log \epsilon$.

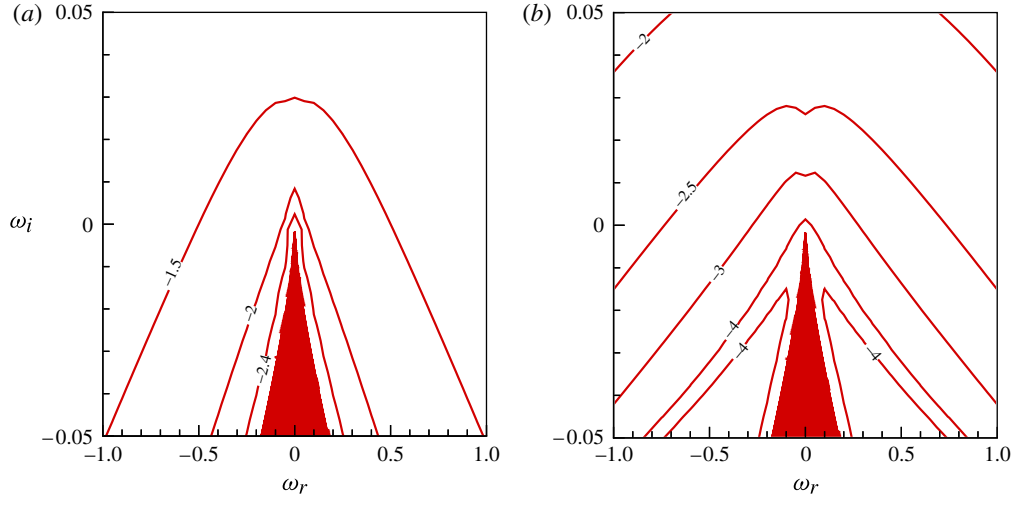

FIGURE 7. (Colour online) Pseudospectra for sliding Couette flow at $Re = 2000$, $\eta = 0.01$. (a) $n = 0$; (b) $n = 1$. The contours represent the level of $\log \epsilon$.

In order to find the characteristics of the response to stochastic external forcing at real frequencies, we plot in figures 8 and 9 the curves of maximum response $\mathscr{R}(\omega)$ versus the frequency ω for $\eta = 0.01$ and 0.5 at $Re = 2000$. In figure 8(a), the maximum response of each curve is realized at the low-frequency limit of $\omega = 0$. The amplitude of the response in the axisymmetric case is much lower than that in the cases of $n = 1, 2, 3$. Of all modes, $n = 1$ has the largest response to external forcing. In figure 8(b), the curves of the streamwise wavenumber corresponding to the most amplified external forcing are plotted. It is found that the wavenumber increases

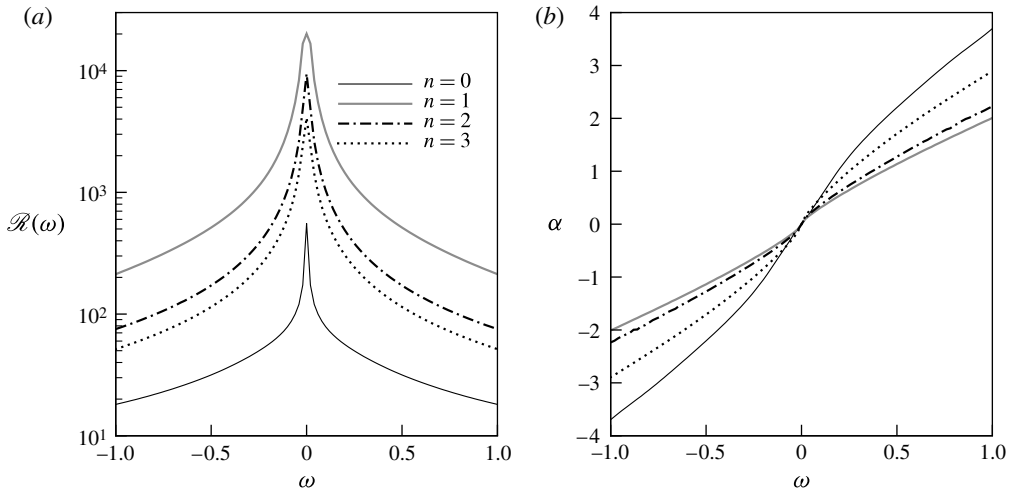

FIGURE 8. (*a*) The curves of the response to continuous external excitations versus the real frequency ω at $Re = 2000$ and $\eta = 0.01$. (*b*) The curves of streamwise wavenumber corresponding to the maximal response at $Re = 2000$.

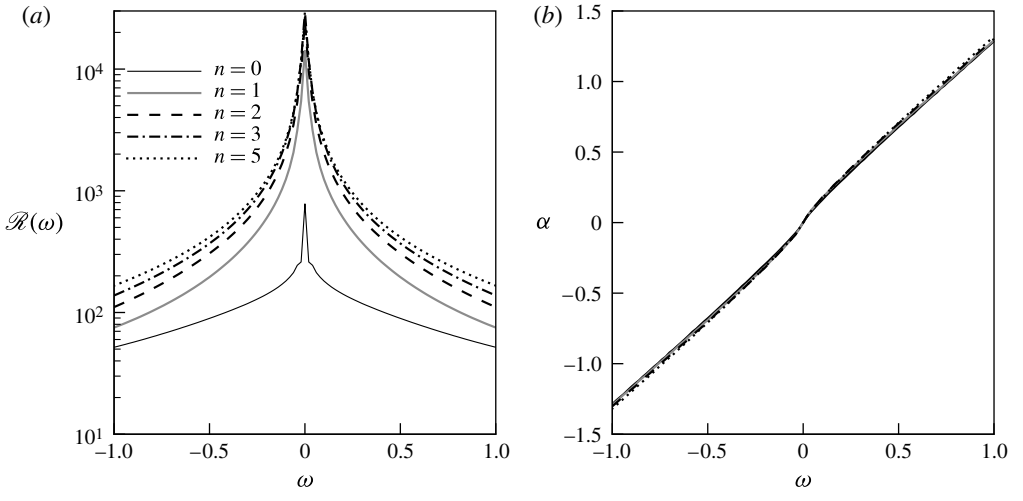

FIGURE 9. (*a*) The curves of the response to continuous external excitations versus the real frequency ω at $Re = 2000$ and $\eta = 0.5$. (*b*) The curves of streamwise wavenumber corresponding to the maximal response at $Re = 2000$.

with the increase of frequency. In the low-frequency range, the curves of streamwise wavenumber are almost indistinguishable for different azimuthal wavenumber n.

In figure 9(*a*), we plot the curves of the maximum response to external forcing with various azimuthal wavenumbers for $\eta = 0.5$ at $Re = 2000$. From $n = 0$ to 5, the axisymmetric external forcing has the lowest amplification of response. As n increases from 0 to 5, the response increases with the increase of n at all frequencies. In figure 9(*b*), curves of the wavenumber corresponding to the maximum response are

almost indistinguishable at all frequencies. The results in figures 8 and 9 indicate that the largest amplification is achieved by time-independent excitations and the response is more sensitive to lower-frequency external forcing. In figures 8(*b*) and 9(*b*), the streamwise wavenumber of the most amplified external forcing is always zero. This result means that the most amplified response is in the form of streamwise-independent streaks.

In order to know more about the physical mechanism of the response to external forcing, we present the spatial structures of the optimal input of spatially harmonic forcing and the output for several typical values of η at $Re = 2000$ in figure 10. As the optimal frequency is $\omega = 0$, only plots of input and output are needed. We have computed the velocity fields of the optimal input and output. The results show that the streamwise components of input disturbances are very weak and the radial and azimuthal velocity components have most of the perturbation kinetic energy. For the optimal output, the magnitudes of radial and azimuthal velocity components are smaller in comparison with the streamwise component. The velocity field $u\boldsymbol{e}_r + v\boldsymbol{e}_\theta$ associated with the optimal input is plotted in figure 10(*a,c,e*) for $\eta = 0.5$, $\eta = 0.1$ and $\eta = 0.01$ at $Re = 2000$. The flow of the input field is characterized by pairs of counter-rotating vortices. The optimal output of the amplitude of the streamwise velocity component w is plotted in figure 10(*b,d,f*) for $\eta = 0.5$, 0.1 and 0.01, showing that the counter-rotating vortices of the input result in streaks of output. The flow fields of the optimal input and output in figure 10 imply that the dominant physical mechanism for the response to excitation is the lift-up effect. From the flow patterns for various values of η, it is found that with the increase of η, the optimal azimuthal wavenumber increases. For different η, the radial size and the azimuthal size of the input vortices and output streaks are comparable. Being similar to the problem of energy stability analysis, we can link the azimuthal wavenumber of the optimal disturbance of SCF to PCF. For SCF, the azimuthal wavenumber of the optimal response to external forcing can be estimated by $n \simeq \beta(1+\eta)/(1-\eta)$, in which β is the spanwise wavenumber of optimal response to external forcing for PCF. For example, for $\eta = 0.5$ the azimuthal wavenumber of the most amplified external excitation is $n = 5$. For $\eta = 0.5$, the estimated value of spanwise wavelength is 1.67 for SCF. This value is very close to $\beta \approx 1.6$ for PCF.

5.2. *Transient growth and optimal disturbances*

In this subsection, we focus on the problem of response to initial conditions. We can define the energy growth maximized over time as:

$$G_{max} = G(t_{max}) = \max_{t \geqslant 0} G(t). \tag{5.9}$$

If the Reynolds number is less than the critical energy Reynolds number Re_1, then $G(t) \leqslant 1$ for all time. In this case, $G_{max} = 1$ and $t_{max} = 0$. If the Reynolds number exceeds the linear critical Reynolds number Re_2 such that the operator $\mathscr{L}$ has an unstable eigenvalue, then $G_{max} \to \infty$ as $t_{max} \to \infty$. If $Re_1 < Re < Re_2$, the flow is linearly stable but has a transient energy growth. For general instability problems, these three types of behaviour should be considered. Deguchi & Nagata (2011) have studied the linear stability of SCF, and found that the flow becomes unstable at rather high Reynolds number of the order of 10^7 for $\eta \leqslant 0.1415$. When examining the characteristics of the transient growth, we only need to consider the case of $Re_1 < Re < Re_2$.

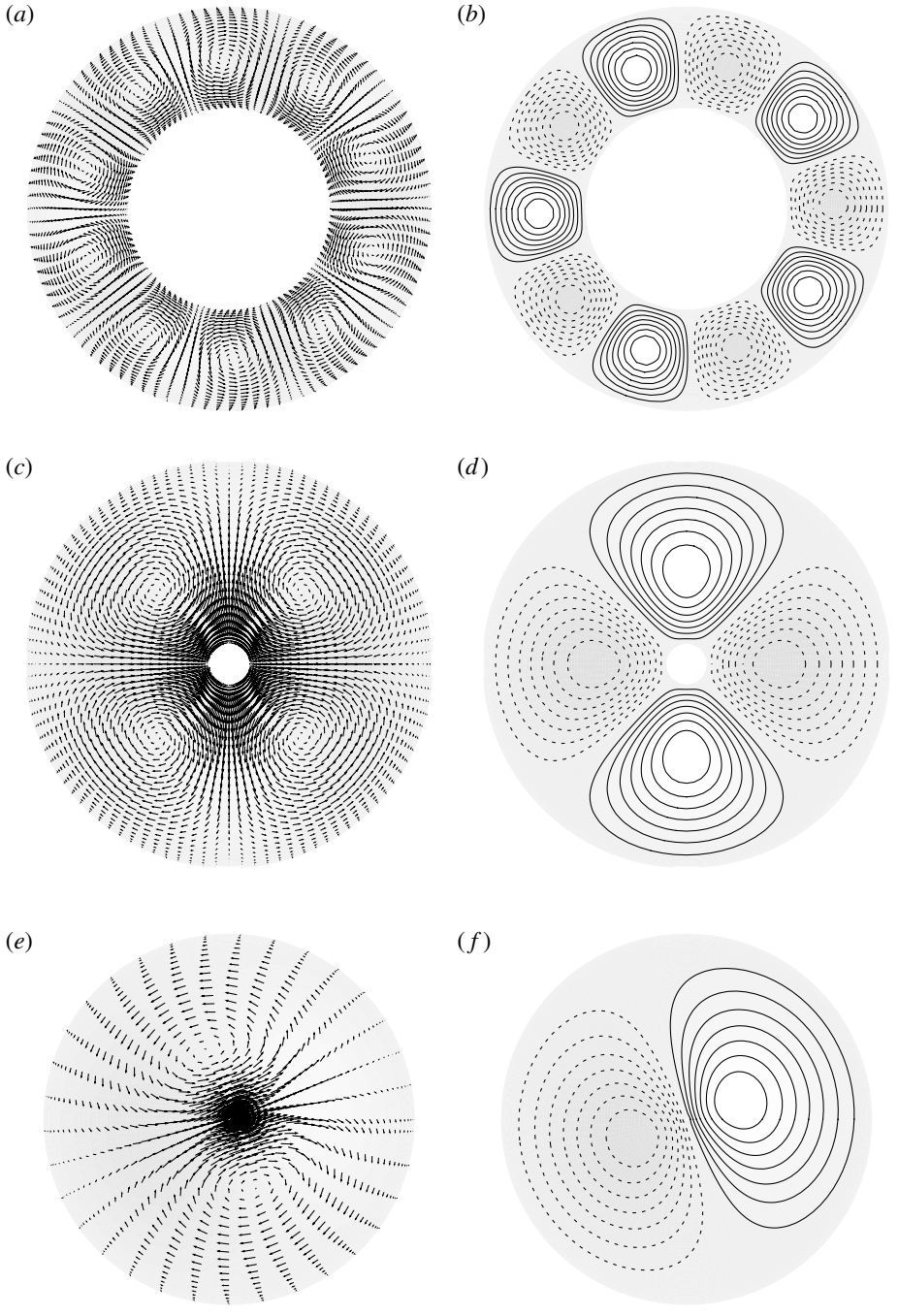

FIGURE 10. Cross-stream (r–θ) view of the optimal input and output flow fields of the response to harmonic forcing at $Re = 2000$, $\alpha = 0$. (a,c,e) The velocity components of u and v of the input. (b,d,f) Isolines of the velocity component w of the output. $\eta = 0.5$ and $n = 5$ for (a,b), $\eta = 0.1$ and $n = 2$ for (c,d), $\eta = 0.01$ and $n = 1$ for (e,f).

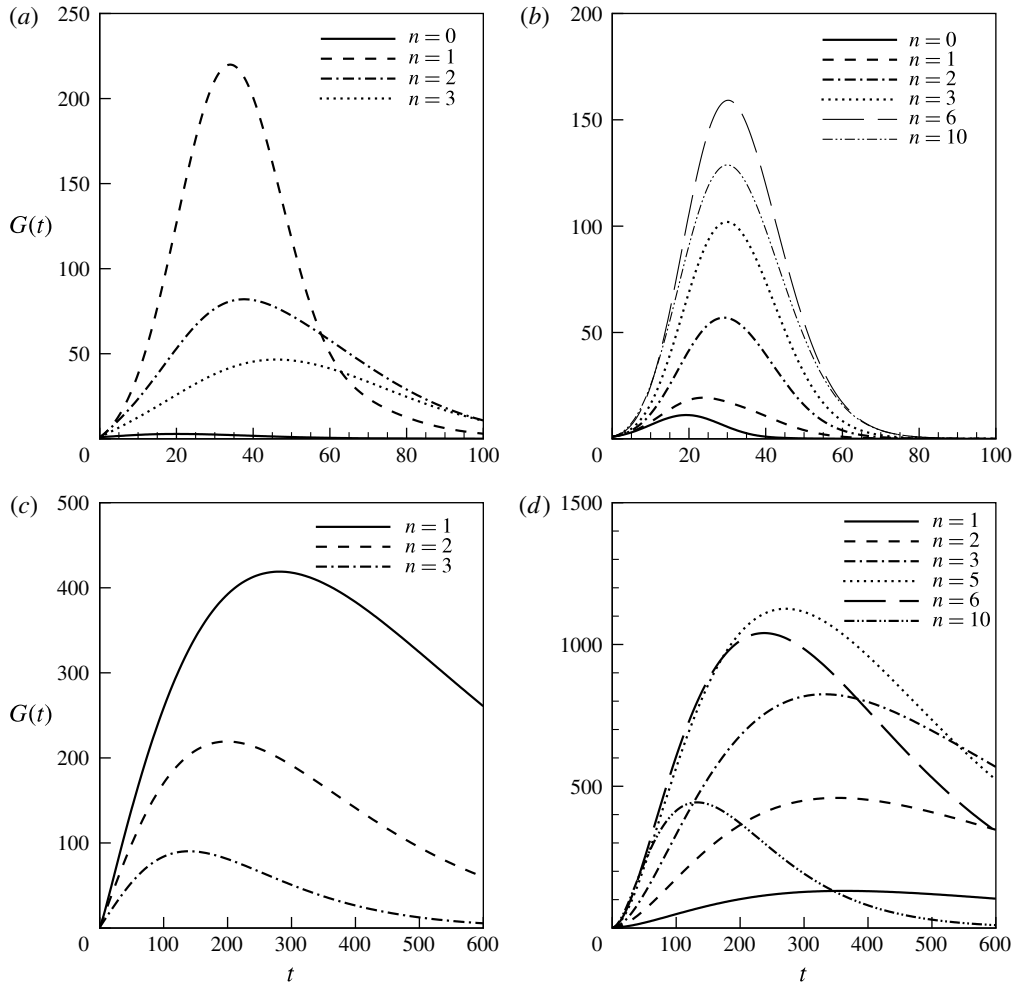

FIGURE 11. The curves of transient energy growth function $G(t)$ versus time t for various azimuthal wavenumbers at $Re = 2000$. (*a*) $\eta = 0.01$, $\alpha = 1.0$; (*b*) $\eta = 0.5$, $\alpha = 1.0$; (*c*) $\eta = 0.01, \alpha = 0$; (*d*) $\eta = 0.5, \alpha = 0$.

In figure 11(*a,b*), the curves of maximum response to initial conditions are plotted for streamwise-dependent disturbances with $\alpha = 1$ at $Re = 2000$ for $\eta = 0.01$ and 0.5. In these two figures, each curve shows that the disturbance experiences a rapid transient growth and then decays after t_{max} because of the effect of viscosity. In the case of $n = 0$, the two-dimensional Reynolds stress mechanism is responsible for the rapid transient growth of the axisymmetric disturbance. In the cases of $n \geqslant 1$, in addition to the two-dimensional Reynolds stress mechanism, the lift-up effect is responsible to the rapid transient energy growth. In figure 11, the amplification of response to disturbances in the axisymmetric case is much lower than that in the non-axisymmetric case. For $\eta = 0.01$, the disturbance of $n = 1$ has the greatest maximum energy growth. For $n \geqslant 1$, with the increase of n, the energy growth decreases in the growth stage. In the viscous stage, the energy growth of $n = 1$ decreases more rapidly than for $n = 2$ and 3. In figure 11(*b*) for $\eta = 0.5$, mode $n = 6$ has the greatest

maximum amplitude of response. For $n \leqslant 6$, with the increase of n the amplitude of response increases. For $n > 6$, the amplitude of response decreases with the increase of n.

In figure 11(*c,d*), the curves of maximum energy growth are plotted for streamwise-independent disturbances. In the case of $\alpha = 0$, the lift-up effect is responsible for the energy growth of the streaks. From (5.6), we can see that for the axisymmetric case of $n = 0$, the effect of stretching of vorticity is absent. Our numerical result also shows that there is no transient energy growth for the axisymmetric case. In figure 11(*c*) for $\eta = 0.01$, the curve of $n = 1$ has the largest maximum energy growth. With the increase of n, both the maximum energy growth and the optimal time t_{max} decrease. This result is different from the case as shown in figure 11(*a*) for $\alpha = 1$ and $n = 1, 2, 3$ in that the optimal time t_{max} increases with the increase of n. In figure 11(*d*) for $\eta = 0.5$, the curve of $n = 5$ has the most amplified response. For $n \leqslant 5$, the maximum response increases with the increase of n. For $n > 5$, the maximum response decreases with the increase of n. In this figure, it is shown that with the increase of n the optimal time t_{max} decreases.

We have examined the transient behaviours of streamwise-independent and streamwise-dependent spatially harmonic disturbances. In order to show the energy growth of spatially stochastic disturbances, we will present the maximal energy growth G_{max} for continuously varying α and various n. Figure 12(*a,b*) displays the curves of G_{max} versus the streamwise wavenumber α with various n at $Re = 2000$. As shown, the structure of the curve of $n = 0$ is significantly different from that of $n \geqslant 1$. For $n = 0$, the transient energy growth is absent in the long-wave range, and the optimal energy growth is achieved by disturbances in the medium- or short-wave range. In this case, the two-dimensional Reynolds stress mechanism is responsible for the transient energy growth. For the non-axisymmetric cases, the disturbance is significantly amplified in the long-wave range and then gradually decreases with the increase of the streamwise wavenumber. In figure 12(*a,b*), it is shown that the streamwise wavenumber of the most amplified disturbance is non-zero in the long-wave range. This means that the optimal response of $n \geqslant 1$ is in the form of slightly oblique streaks.

In order to show the influence of the Reynolds number on the optimal response to initial conditions, we plot in figure 12(*c,d*) the curves of the optimal response for $\eta = 0.5$, $n = 5$ and 0.01, $n = 1$ at various Reynolds numbers. It is apparent that the response increases with the increase of the Reynolds number at all streamwise wavenumbers. At low Reynolds number of $Re = 500$, the optimal response is realized at $\alpha \simeq 0.2$ and 0.5 for $\eta = 0.5$ and 0.01, respectively. With the increase of the Reynolds number, the optimal streamwise wavenumber decreases. At the high Reynolds number of $Re = 10\,000$, the optimal streamwise wavenumber is very close to zero. In this case, the optimal response is close to streamwise-independent streaks. We have computed the energy growth for the optimal initial disturbances in the form of streamwise vortices at a wide range of Reynolds numbers for different radii ratios η. It is found that the relationship $G(t)/Re^2 = f(t/Re)$ is always satisfied. Having obtained the energy growth function $G(t)$ at $Re = 2000$, we can obtain the energy growth at different Re from this relationship.

The results of the dependence of optimal growth of streamwise-independent disturbance on Reynolds number are summarized in table 2. We have computed the optimal transient energy growth together with the optimal time for a wide range of radius ratios. It is shown that for each η, at high Reynolds numbers the optimal energy growth is of order Re^2 and the optimal time is proportional to Re. For the narrow-gap case of $\eta \geqslant 0.5$, the relation between G_{max} and Re is quantitatively close to that for

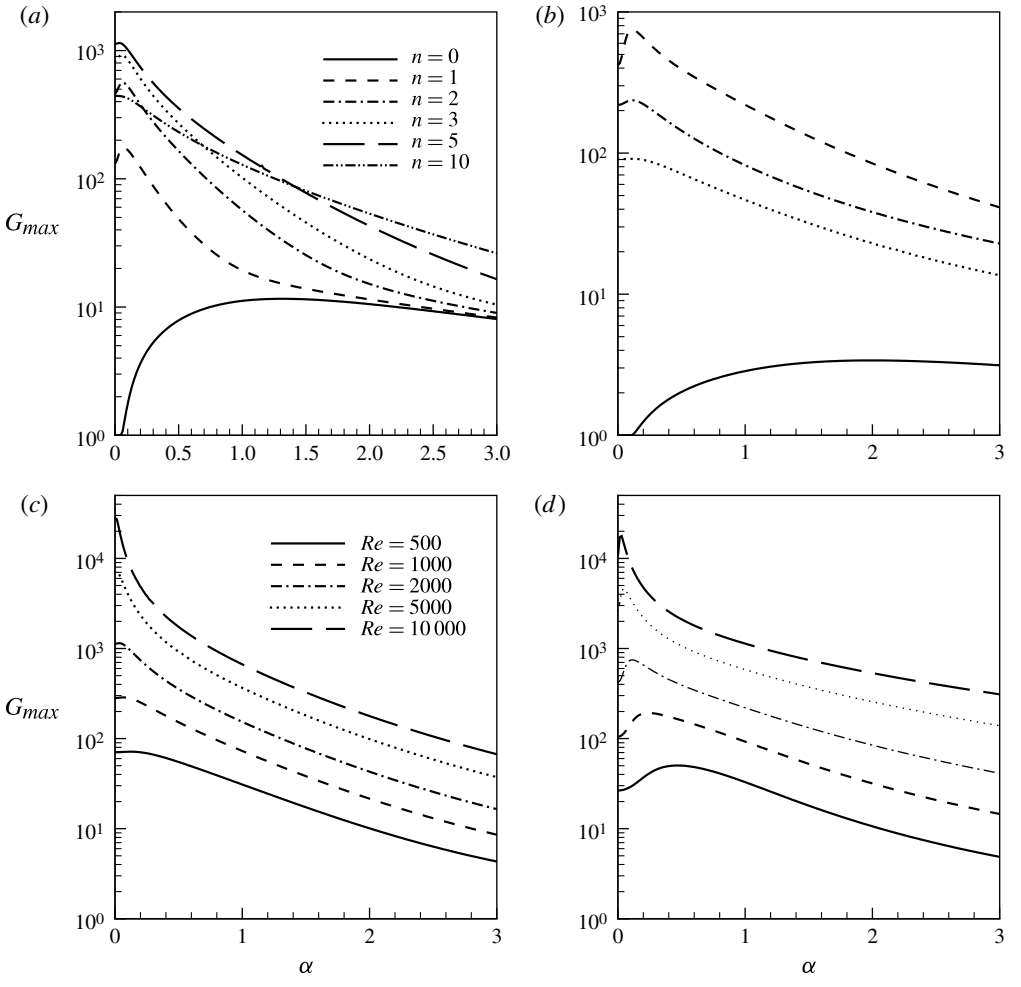

FIGURE 12. The maximum transient energy growth G_{max} versus the streamwise wavenumber α. (*a*) $\eta = 0.5$ and (*b*) $\eta = 0.01$ for various n at $Re = 2000$; (*c*) $\eta = 0.5$, $n = 5$ and (*d*) $\eta = 0.01$, $n = 1$ for various Re.

	η	n		$G_{max}(10^{-4})$	t_{max}
	0.01	1	0	$1.06Re^2$	$0.142Re$
	0.1	2	0	$1.93Re^2$	$0.122Re$
	0.5	5	0	$2.81Re^2$	$0.122Re$
	0.8	15	0	$2.90Re^2$	$0.138Re$
	0.98	164	0	$2.90Re^2$	$0.138Re$
PCF	—	—	0	$2.91Re^2$	$0.141Re$

TABLE 2. Reynolds number dependence of G_{max} and t_{max}, for $\alpha = 0$, for a sliding Couette flow in comparison with that of a plane Couette flow.

plane Couette flow. It is interesting that the relation between G_{max} and Re for SCF is qualitatively similar to that for other shear flows, such as plane Couette flow, plane Poiseuille flow and Hagen–Poiseuille flow.

In order to know more about the physical mechanism for the energy growth of optimal disturbances, we plot the flow fields for two typical cases: the azimuthal-independent and the streamwise-independent disturbances. Figure 13 displays isolines of the streamfunction of the axisymmetric optimal disturbances at the initial stage, at the optimal time and after the optimal time for $\eta = 0.01$ and 0.5 at $Re = 2000$. As shown in figure 13(*a,b*), the vortex structure of the initial flow field tilts opposite to the mean flow. As explained by the two-dimensional Reynolds stress mechanism, the disturbance gains energy from the mean shear. Comparing figure 13(*a*) with 13(*b*), it is observed that with the increase of η, the vortex tilts further in the direction opposite to the mean flow. This means that for a narrower-gap case, the disturbance can extract more energy from the mean flow at the initial stage. As shown in figure 13(*c,d*), at the optimal time the flow patterns become upright. In this case, the disturbance gains no energy from the mean shear. For $\eta = 0.01$ the centre of the circulation is located near the outer cylinder, and for $\eta = 0.5$ it is located near $r = (r_i + r_o)/2$. This means that the mean shear near the outer cylinder provides more energy than that near the inner cylinder for a wide-gap case. After the optimal time, as shown in figure 13(*e,f*) the vortex structure tilts towards the streamwise direction. At this stage, the disturbance energy is returned to the mean flow.

In figure 14, we plot the flow fields of the optimal streamwise-independent disturbance for various η at $Re = 2000$. At the initial time $t = 0$ and optimal time $t = t_{max}$, the flow fields are characterized by pairs of counter-rotating vortices and optimal streaks. For the wide-gap cases of $\eta = 0.01$ and 0.1, the centre of the streak is located near the inner wall. For the narrow-gap case of $\eta = 0.5$, it is located near $r = (r_i + r_o)/2$. As discussed above, the lift-up effect is responsible for the energy growth of the streamwise-independent disturbance. Being different from the two-dimensional Reynolds stress mechanism, in the wide-gap case, the mean shear near the inner wall provides more energy to the disturbance than near the outer wall because the velocity gradient of the base flow is larger near the inner wall than near the outer wall. Comparing each part of figure 14 with those in figure 10, we find that the structures of the initial and optimal flow fields in figure 14 are very similar to those of the response to external forcing shown in figure 10. Being similar to the problem of the response to external forcing, at the initial time, the kinetic energy of the flow is mainly in the components u and v. At the optimal time, it is contained mainly in the w component. For example in the cases of $\eta = 0.01$, 0.1 and 0.5, the ratios of the kinetic energy of w to that of u and v are 0.0667 %, 0.0288 % and 0.0206 % at the initial time, and 99.98 %, 99.99 % and 99.99 % at the optimal time.

For streamwise-dependent disturbances, both the lift-up effect and the two-dimensional Reynolds stress mechanism are responsible for the transient growth of the disturbances. In figure 12(*c,d*), we observed that at low Reynolds numbers, the optimal response is in the form of oblique streaks instead of streamwise streaks. In order to find the effect of the streamwise wavenumber on the energy growth, we list in table 3 two energy ratios at the initial time and the optimal time at $Re = 2000$: the ratio of the energy in the u, v components and the total kinetic energy; and the ratio of the energy in the w component and the total kinetic energy. For $\eta = 0.01$ and $\alpha = 0.3$, at the initial time, 95.43 % of the kinetic energy is in u and v. At the optimal time, 95.95 % of the kinetic energy is in w. These two ratios are lower than those of streamwise-independent case. As α increases to 1.0, these two ratios decrease to

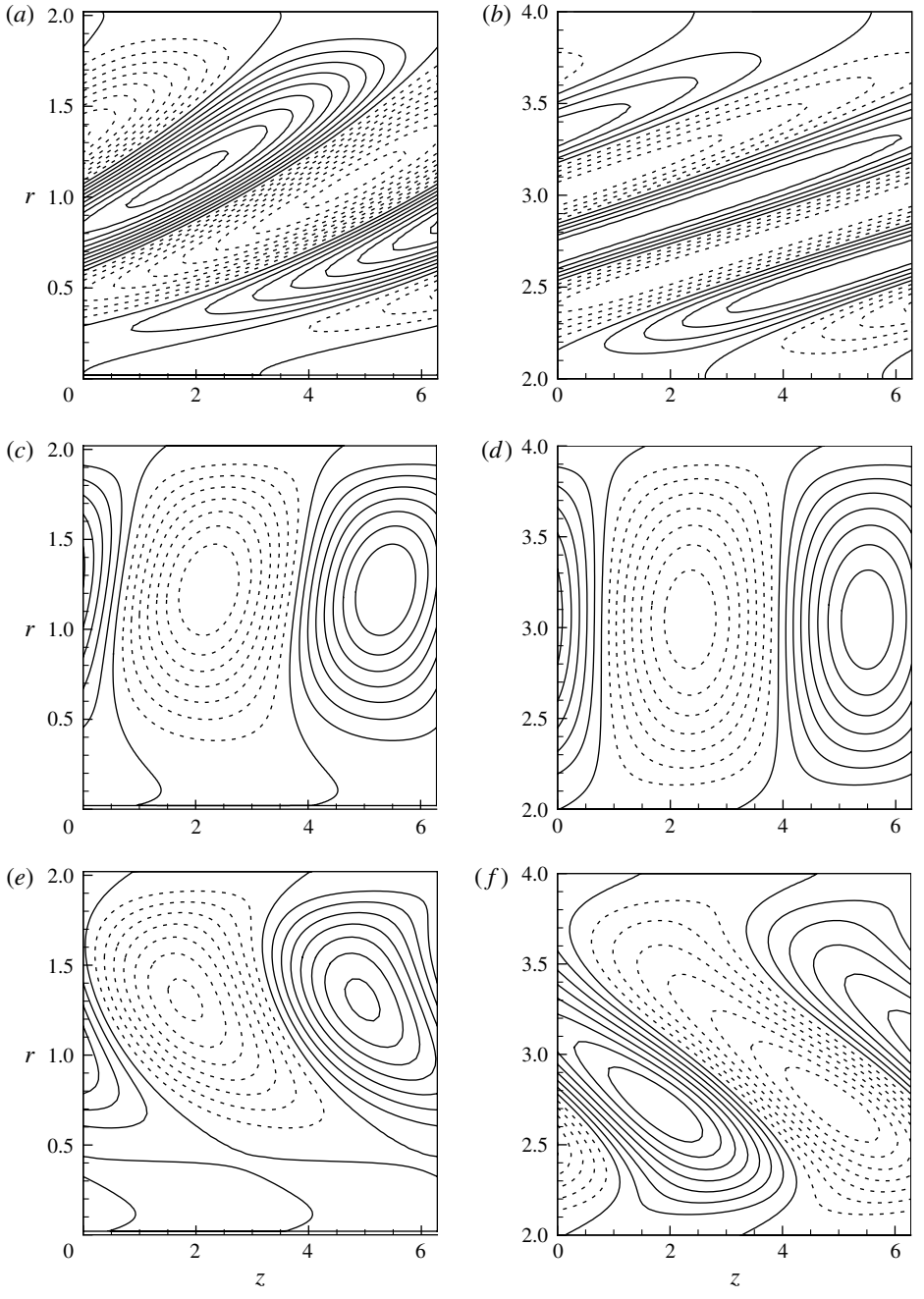

FIGURE 13. An $(r$–$z)$ view of the flow patterns of the streamfunction for the optimal axisymmetric disturbance at $Re = 2000$. (a,b) Flow field at the initial time $t = 0$; (c,d) flow field at the optimal time ($t = 20.1$ and $t = 19.3$ resp.) ; (e,f) flow field after the optimal time ($t = 40$ and $t = 30$ resp.). (a,c,e) $\eta = 0.01$, $G_{max} = 2.85$, $t_{max} = 20.1$, $\alpha = 1.0$; (b,d,f) $\eta = 0.5$, $G_{max} = 11.17$, $t_{max} = 19.3$, $\alpha = 1.0$. For $\eta = 0.01$, $r_i = 0.0202$, $r_o = 2.0202$; for $\eta = 0.5$, $r_i = 2$, $r_o = 4$.

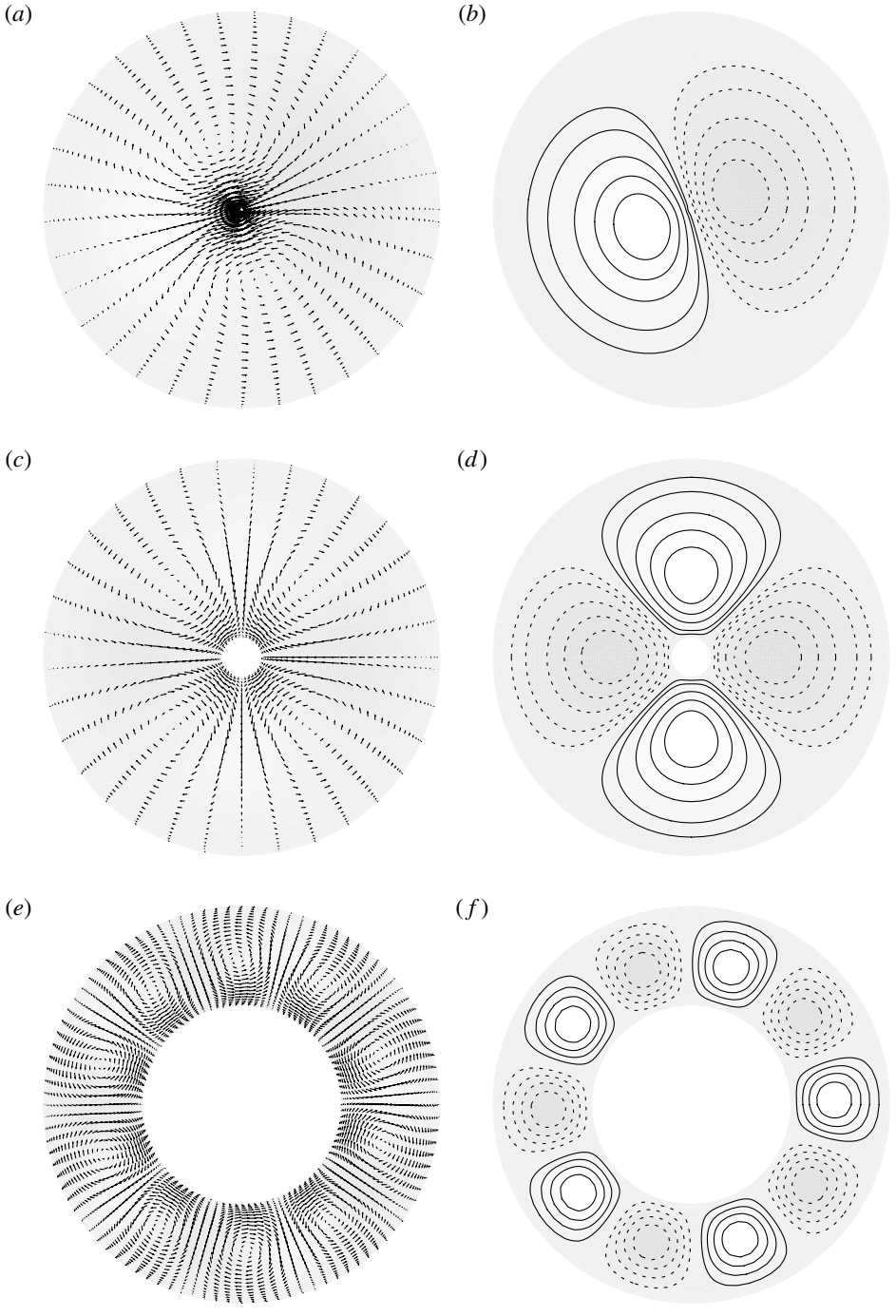

FIGURE 14. The cross-stream (r–θ) view of the optimal input and output flow fields of the response to initial conditions at $Re = 2000$, $\alpha = 0$. (a,c) The velocity components of u and v of the input. (b,d) Isolines of the velocity component w of the output. $\eta = 0.01$ and $n = 1$ for (a,b), $\eta = 0.1$ and $n = 2$ for (c,d), $\eta = 0.5$ and $n = 5$ for (e,f).

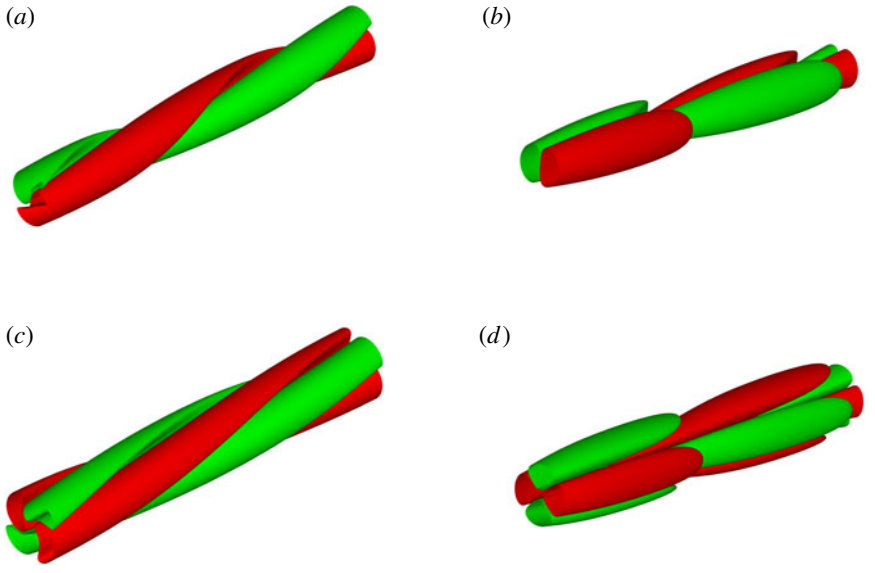

FIGURE 15. (Colour online) Isosurfaces of the axial component of the disturbance velocity of the streaks at the optimal time. (*a*) Mode $n = 1$; (*b*) combination of modes of $n = \pm 1$ for $\eta = 0.01$; (*c*) mode $n = 2$; (*d*) combination of modes of $n = \pm 2$ for $\eta = 0.1$. Other parameters are $Re = 500$ and $\alpha = 0.3$. The red (dark grey in print) and green (light grey in print) surfaces correspond to the fast and the slow streaks, respectively.

η	n	α	$\frac{E_{u,v}(0)}{E(0)}$	$\frac{E_w(0)}{E(0)}$	$\frac{E_{u,v}(t_{max})}{E(t_{max})}$	$\frac{E_w(t_{max})}{E(t_{max})}$
0.01	1	0	0.9993	6.67×10^{-4}	2.28×10^{-4}	0.9998
0.01	1	0.3	0.9543	0.0457	0.0405	0.9595
0.01	1	1.0	0.8415	0.1585	0.1597	0.8403
0.1	2	0	0.9997	2.88×10^{-4}	1.36×10^{-4}	0.9999
0.1	2	0.3	0.9725	0.0275	0.0307	0.9693
0.1	2	1.0	0.8402	0.1598	0.1878	0.8122
0.5	5	0	0.9998	2.06×10^{-4}	6.66×10^{-5}	0.9999
0.5	5	0.3	0.9646	0.0354	0.0417	0.9583
0.5	5	1.0	0.7275	0.2725	0.3185	0.6815

TABLE 3. The energy ratios at the initial time and optimal time at $Re = 2000$.

84.15 % and 84.03 %. For other radius ratios, the effect of the streamwise wavenumber on the energy ratios at the initial time and the optimal time is similar to that of $\eta = 0.01$. In table 3, for the streamwise wavenumber in the range from 0 to 1.0, at the optimal time the kinetic energy is mainly in the streamwise component w. This means that the optimal disturbance is in the form of straight streaks or helical streaks.

For a streamwise-independent disturbance, at the optimal time the disturbance is in the form of streaks parallel to the axial direction. For a streamwise-dependent disturbance, the optimal disturbance of $n \neq 0$ is in the form of helical streaks. For each pair of wavenumbers (α, n), if $(\hat{\Phi}, \hat{\Omega})$ satisfy the controlling equations, it can be

shown that $(\hat{\Phi}, -\hat{\Omega})$ is the solution for $(\alpha, -n)$. So, in computation we only consider the case of positive azimuthal wavenumber n. For $(\alpha, -n)$, the components of u and w are identical to the solution for (α, n) and the component of v has the opposite sign to that of (α, n). If we combine the optimal disturbances of $\pm n$, we can obtain another form of streaks. The isosurfaces of the streamwise velocity component of the optimal disturbance at the optimal time are shown in figure 15. The structures of optimal response in the form of helical streaks are shown in figure 15(*a,c*) for $\eta = 0.01$ and 0.1, respectively. The structures of the response of combination modes are shown in figure 15(*b,d*) for $\eta = 0.01$ and 0.1, and are in the form of streamwise-dependent straight streaks.

6. Nonlinear evolution of the optimal disturbances

In this section, we will investigate the streak breakdown phase and the transition initiated by streamwise vortices in the SV scenario via a direct numerical simulation. We solve the incompressible Navier–Stokes equations with the velocity components u, v, w and the pressure p as the independent variables. A time-splitting method is used for solving the momentum equation and imposing the divergence-free condition in the three fractional steps. The temporal integration is based on the Crank–Nicholson scheme for the viscous terms and the second-order Adams–Bashforth scheme for the nonlinear terms. The flow variables are expanded in terms of truncated Fourier series in the streamwise and azimuthal directions and Chebyshev polynomials in the radial directions. Splitting methods in conjunction with Fourier–Chebyshev spectral method have been used with success in simulating the nonlinear evolution in plane channel and pipe Poiseuille flows (Orszag & Kells 1980; Orszag & Patera 1983). The flow is assumed to be periodic in the streamwise and azimuthal directions, with the fundamental streamwise and azimuthal wavenumbers α and the n. The energy density of a disturbance is given by

$$E = \frac{1}{2V} \iiint_{period} (u^2 + v^2 + w^2) 2\pi r \, \mathrm{d}r \, \mathrm{d}\theta \, \mathrm{d}z, \tag{6.1}$$

where the region of integration is one periodic box, and V is the volume of the periodic box. The amplitude of the disturbance is defined as $\varepsilon = (E/2)^{1/2}$.

We begin by examining the formation of streamwise streaks generated by the nonlinear evolution of the optimal streamwise vortices. The time evolution of the energy of optimal streamwise vortices with finite amplitude is shown in figure 16 for various η at $Re = 1000$. The initial condition is given by the streamwise-uniform vortices predicted by linear non-modal analysis. The amplitudes of initial disturbances ε vary from 0.001 to 0.05. In figure 16(*a–c*), for the low value of $\varepsilon = 0.001$ the contribution of the nonlinear terms is slight. The curves of $\varepsilon = 0.001$ almost coincide with the curves of the linear optimal disturbances. For larger amplitudes of $\varepsilon \geqslant 0.01$, at small t the growth of the energy is mainly due to the linear transient mechanism. So, as shown in figure 16, at initial stage the nonlinear curve for $\varepsilon \geqslant 0.01$ follows the linear curve. Because of the streamwise independence of the optimal vortices, the rolls have no energy source. The flow undergoes a viscous decay after the initial transient growth and the disturbances are eventually damped. In each of figures 16(*a*) to 16(*c*), both the amplification of the energy of disturbance and the maximum growth time t_{max} decrease with the increase of ε. Comparing the curves for $\varepsilon = 0.05$ with different η it is obvious that in the wide-gap case the amplification of the energy of optimal disturbance is lower than that in narrow-gap cases.

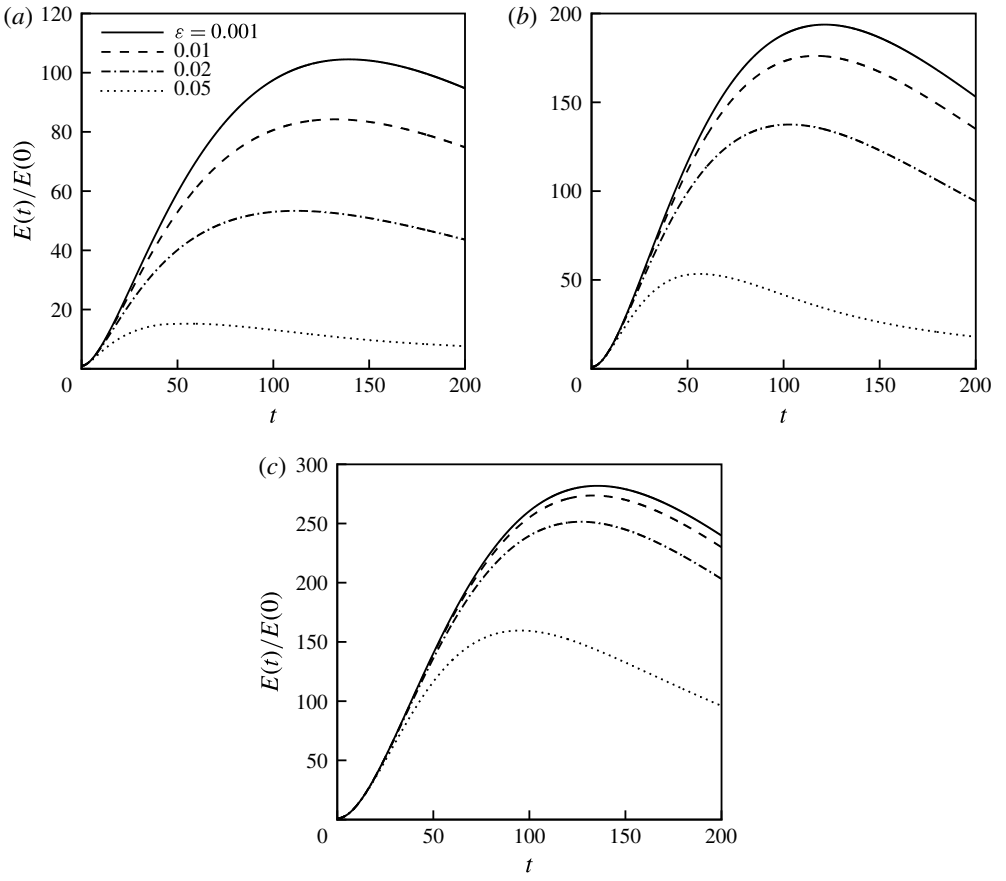

FIGURE 16. Time evolution of the amplification of kinetic energy associated with optimal streamwise vortices at $Re = 1000$. (*a*) $\eta = 0.01$, $n = 1$; (*b*) $\eta = 0.1$, $n = 2$; (*c*) $\eta = 0.5$, $n = 5$. The grid is composed of $16 \times 16 \times 32$ physical grid points in the streamwise, azimuthal and radial directions.

Streaky structures elongated in the streamwise direction play a fundamental role in the transition and the sustainment of turbulence in wall-bounded shear flows. The amplitude of the initial disturbance is an important factor in the formation of streaky structures. In figure 17, we present contours of the streamwise velocity at $Re = 1000$ for various η with $\varepsilon = 0.01$ and 0.05. In figure 17(*a,c,e*) for $\varepsilon = 0.01$, it is obvious that the contours have been distorted with respect to the base state. As ε increases to 0.05, streamwise streaks of high- and low-speed fluid have been formed by the lift-up mechanism and modified by the nonlinear effect.

If the streak amplitude is sufficiently large, the streaks can break down. The breakdown of streaks is similar to a Kelvin–Helmholtz instability. In plane Couette and Poiseuille flows, as the vortices evolve, the streamwise velocity profile of streaks develops inflection points in both the normal and spanwise directions. It has been shown that streak breakdown is primarily a spanwise inflectional instability (Reddy *et al.* 1998). In previous works, two approaches have been used to investigate the instability of streaks: linear stability analysis and direct numerical simulation. Waleffe (1995) have studied the breakdown of streaks in plane channel flows using a linear

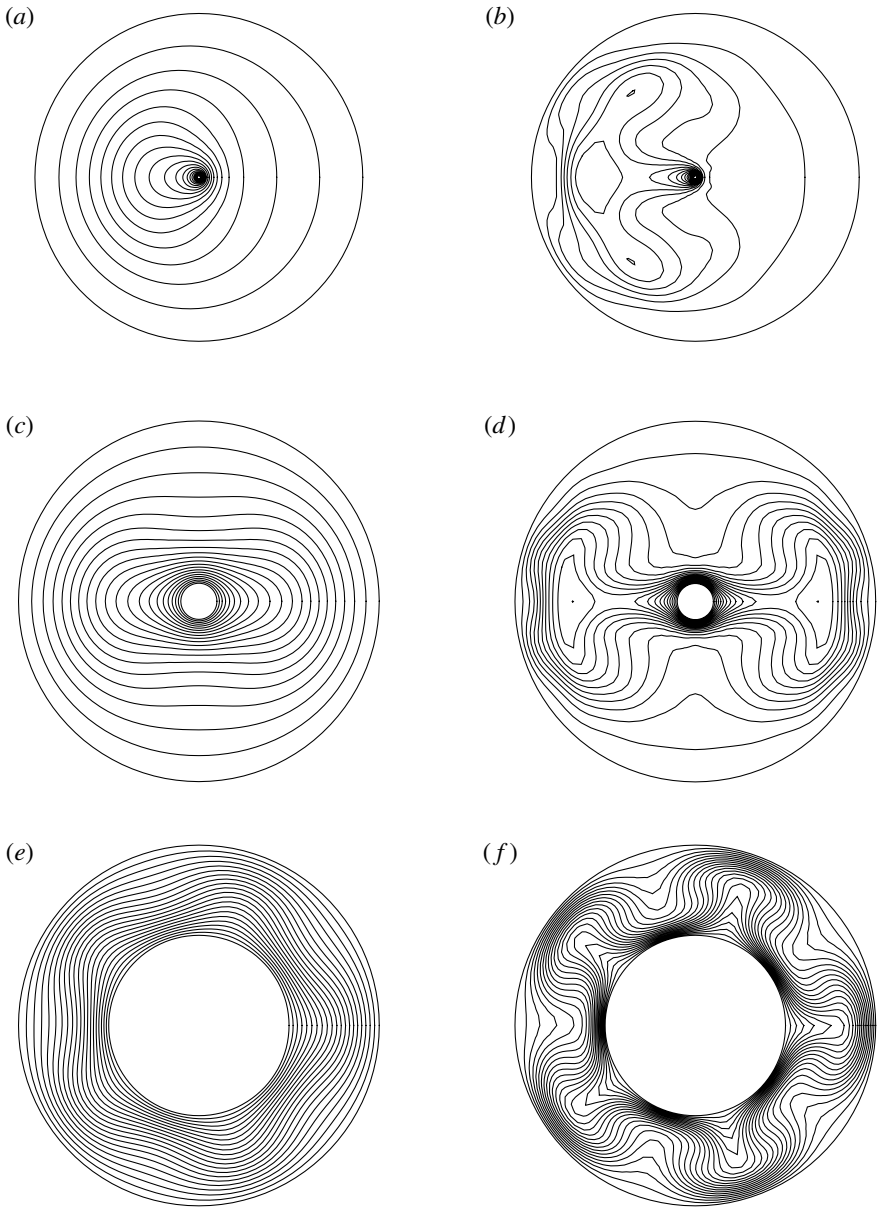

FIGURE 17. Contours of the streamwise velocity of the streaky structure at $Re = 1000$. (*a*) $\eta = 0.01$, $n = 1$ at $t = 100$; (*b*) $\eta = 0.01$, $n = 1$ at $t = 50$; (*c*) $\eta = 0.1$, $n = 2$ at $t = 100$; (*d*) $\eta = 0.1$, $n = 2$ at $t = 50$; (*e*) $\eta = 0.5$, $n = 5$ at $t = 150$; (*f*) $\eta = 0.5$, $n = 5$ at $t = 100$. (*a,c,e*) $\varepsilon = 0.01$; (*b,d,f*) $\varepsilon = 0.05$. The grid is composed of $16 \times 16 \times 32$ physical grid points in the streamwise, azimuthal and radial directions.

stability analysis. In this analysis, it is assumed that the time scale for decay of streaks is longer than the time scale for streak instability. Thus, the streak velocity profile at fixed t is assumed to be steady and used as the base state. Hamilton *et al.* (1995) studied the streak breakdown phase via a direct numerical simulation.

Reddy *et al.* (1998) used both approaches to study the instability of streaks in plane channel flows. The results have shown that the time growth rate obtained via linear stability analysis is consistent with that obtained via direct numerical simulation.

Having examined the formation of streaky structures, we now examine the instability of streaks generated by the initial optimal vortices via a direct numerical simulation. In order to investigate the instability of streaks, we add a disturbance of the form

$$\boldsymbol{v}' = \sum_{k=-K}^{K} \sum_{m=-M}^{M} F_{mk}(r, t) \mathrm{e}^{\mathrm{i}m\alpha z} \mathrm{e}^{\mathrm{i}kn\theta} \tag{6.2}$$

to the streamwise vortices at the initial time. The functions F_{mk} are linear combinations of Stokes modes (Reddy *et al.* 1998). The initial energy density of each mode is 10^{-12}.

In figure 18, we present the evolution of the energy density of the disturbance of various modes with $m = 1$ at $Re = 1000$. In figure 18(*a*) for $\eta = 0.01$, the initial amplitude of the streamwise vortices is $\varepsilon = 0.01$. At the initial stage, some modes of disturbances experience a transient growth and then rapidly decrease with time. In figure 16(*a*), after $t \approx 50$ the energy of streamwise vortices was shown to have significantly increased. In figure 18(*a*) for $\varepsilon = 0.01$, it is observed that with the increase of the amplitude of streaks, all modes experience an exponential growth after $t \approx 50$. This means that as the amplitude of streaks increases to a high value, they can become unstable. In figure 16, the energy of the streaks decreased with time after it reached its maximum value. In figure 18(*a*), it is observed that the energy of all modes eventually decreases with time due to the decrease of the amplitudes of the streaks. In figure 18(*b*), the evolution of the energy density is plotted for $\eta = 0.01$ and $\varepsilon = 0.05$. Comparing figures 18(*a*) and 18(*b*) it is shown that with the increase of ε the energy of each mode increases more rapidly. In figure 18(*c,e*), the evolution of the energy density for various modes is plotted for $\eta = 0.1$ and 0.5 with $\varepsilon = 0.01$, and shows that the energy of all modes significantly decreases with time after the initial stage. This result means that the streaks generated by vortices with $\varepsilon = 0.01$ are stable for $\eta = 0.1$ and 0.5 at $Re = 1000$. In figure 18(*d,f*) for $\varepsilon = 0.05$, after an initial transient phase, the energy density grows with the increase of the amplitude of streamwise streaks. Comparing figure 18(*c*) with 18(*d*) and 18(*e*) with 18 (*f*), it is shown that for $\eta = 0.1$ and 0.5, at $Re = 1000$ the initial amplitude of $\varepsilon = 0.01$ is not sufficient to trigger the secondary instability; however, $\varepsilon = 0.05$ is sufficient. Comparing figure 18(*a*) with 18(*c*) and 18(*e*), it is shown that although the potential of the energy growth of streamwise vortices for the wide-gap case is lower than for the narrow-gap case, the threshold energy of the initial disturbance for triggering secondary instability of streaks is lower for the wide-gap than narrow-gap cases.

The streak instability is necessary but not sufficient for transition. We will explore the transition to turbulence triggered by the nonlinear evolution of the optimal streamwise vortices. To trigger the transition, weak three-dimensional noise is added to the optimal vortices at the initial time $t = 0$. The initial energy density of each mode of the noise is 10^{-12}. In figure 19, the nonlinear evolution of energy growth of disturbances with $\varepsilon = 0.05$ is presented for $\eta = 0.1$ and 0.5. At $Re = 1000$, as shown in figure 18(*d,f*) the streaks generated by optimal vortices of $\varepsilon = 0.05$ are unstable. However, no transition to turbulence was detected at $Re = 1000$ in figure 19(*a,b*). In figure 19(*c,d*), it is observed that the growth of the energy of noise is followed by decay and eventual relaminarization. This result indicates that for streamwise vortices with $\varepsilon = 0.05$, $Re = 1000$ is not sufficient to trigger transition. As shown in figure 19(*a,b*), at $Re = 1500$ transition has been triggered and the energy of

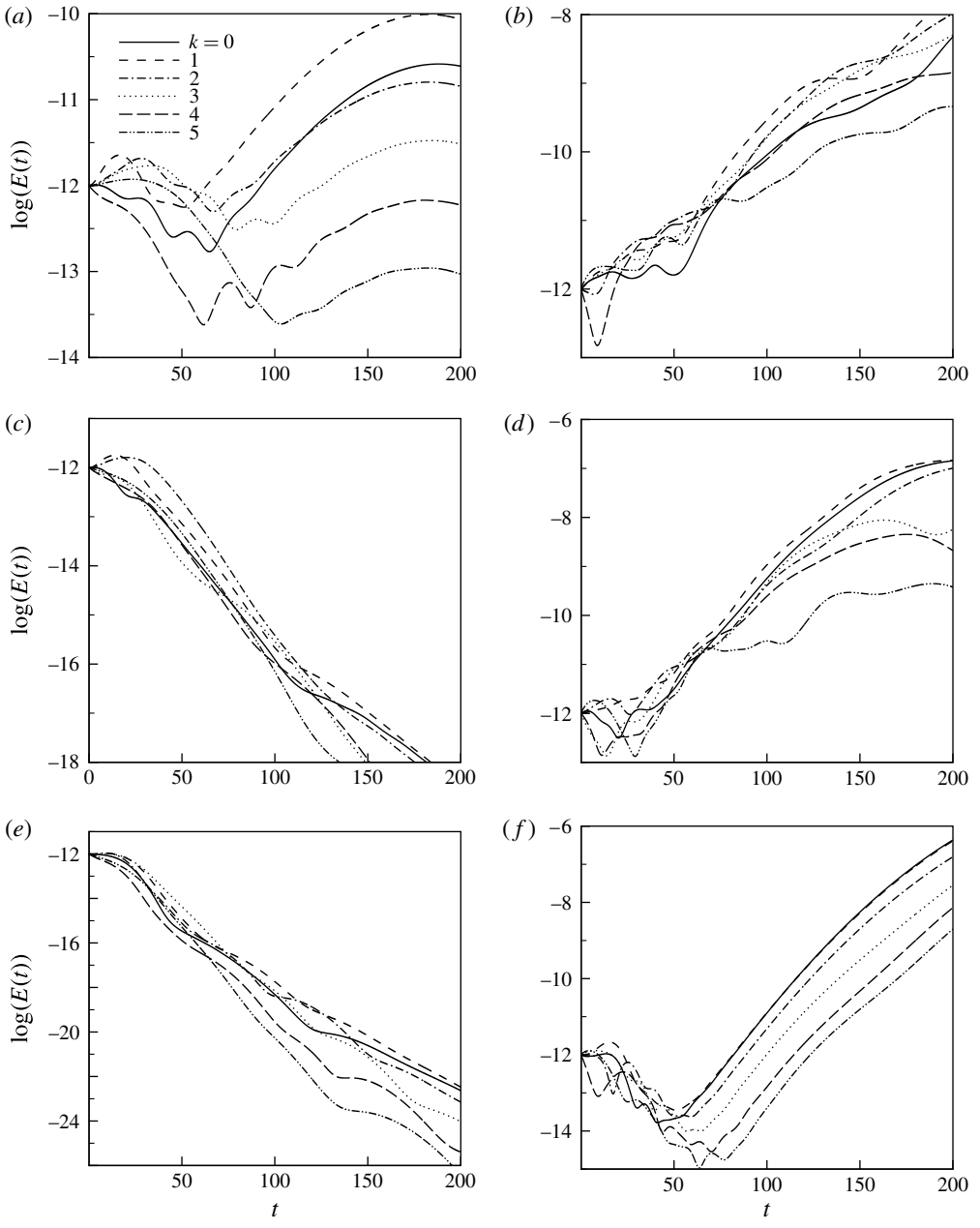

FIGURE 18. Evolution of the energy density for disturbances with wavenumbers (α, kn). (*a*) $\eta = 0.01$, $\varepsilon = 0.01$, $n = 1$; (*b*) $\eta = 0.01$, $\varepsilon = 0.05$, $n = 1$; (*c*) $\eta = 0.1$, $\varepsilon = 0.01$, $n = 2$; (*d*) $\eta = 0.1$, $\varepsilon = 0.05$, $n = 2$; (*e*) $\eta = 0.5$, $\varepsilon = 0.01$, $n = 5$; (*b*) $\eta = 0.5$, $\varepsilon = 0.05$, $n = 5$. The Reynolds number $Re = 1000$, and the streamwise wavenumber $\alpha = 1$. The grid is composed of $16 \times 16 \times 32$ physical grid points in the streamwise, azimuthal and radial directions.

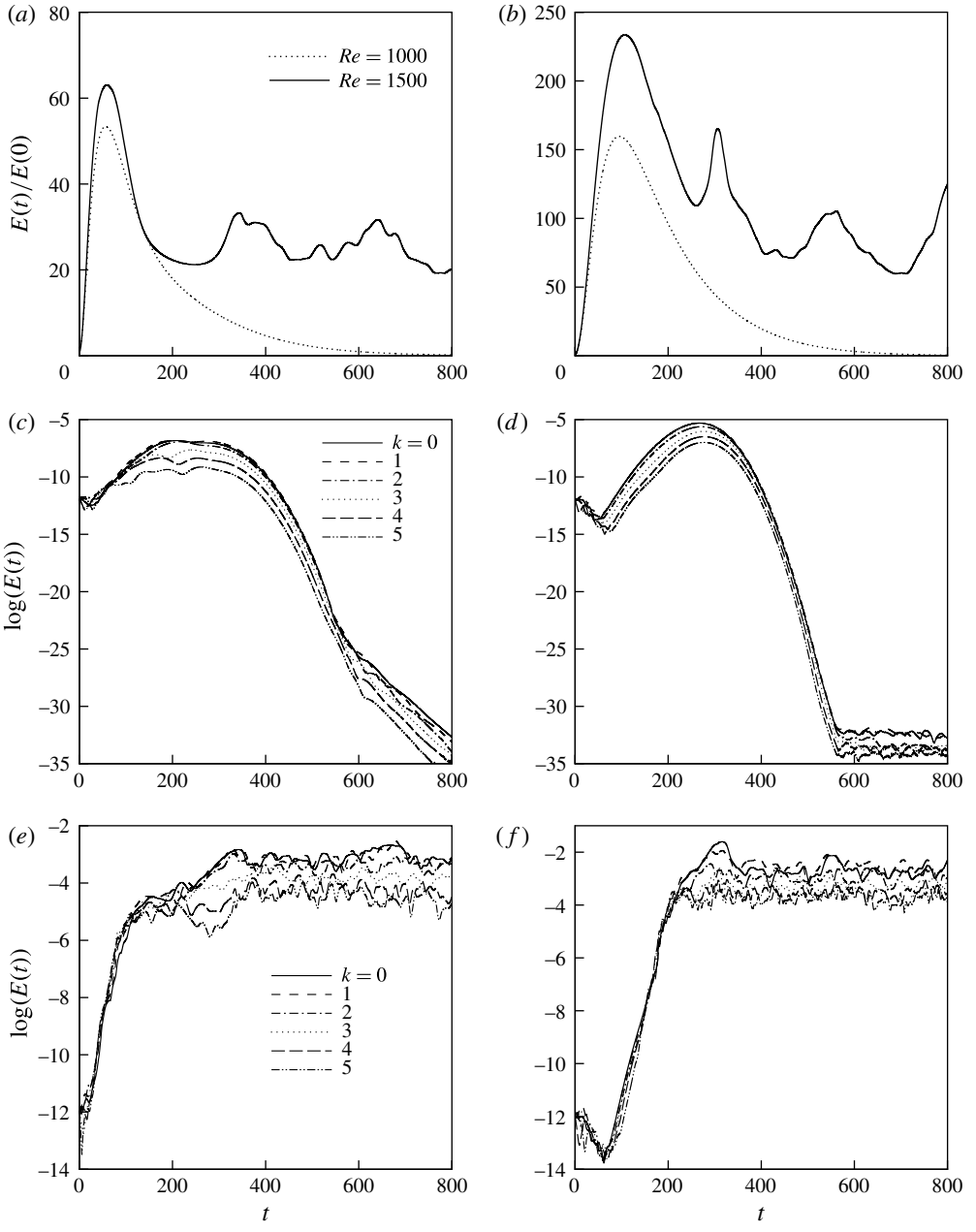

FIGURE 19. Time evolution of the amplification of the energy of disturbances. The initial conditions are given by optimal streamwise vortices with noise for (*a*) $\eta = 0.1$ and (*b*) $\eta = 0.5$ at both $Re = 1000$ and 1500. (*c–f*) Evolution of the energy density for disturbances with wavenumbers (α, kn). (*c*) $\eta = 0.1$, $n = 2$, $Re = 1000$; (*d*) $\eta = 0.1$, $n = 2$, $Re = 1500$; (*e*) $\eta = 0.5$, $n = 5$, $Re = 1000$; (*f*) $\eta = 0.5$, $n = 5$, $Re = 1500$. The streamwise wavenumber $\alpha = 1$, the amplitude of initial optimal streamwise vortices $\varepsilon = 0.05$. The grid is composed of $16 \times 16 \times 32$ physical grid points in the streamwise, azimuthal and radial directions.

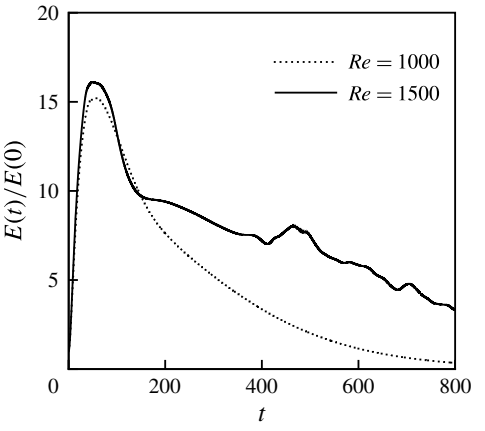

FIGURE 20. Time evolution of the amplification of the energy of disturbances. The initial conditions are given by optimal streamwise vortices with noise for $\eta = 0.01$. The streamwise wavenumber $\alpha = 1$, the amplitude of initial optimal streamwise vortices $\varepsilon = 0.05$. The grid is composed of $16 \times 16 \times 32$ physical grid points in the streamwise, azimuthal and radial directions.

the disturbances can be sustained. In figure 19(*e*,*f*), transition has been observed at $t \approx 120$ and 200 for $\eta = 0.1$ and 0.5, respectively. Comparing the curves with $Re = 1500$ in figure 19(*a*,*b*) it is found that for $\eta = 0.1$ the energy of the disturbances can be sustained in a lower level than that for $\eta = 0.5$.

In figure 20, the nonlinear evolution of energy growth of disturbances with $\varepsilon = 0.05$ is presented for $\eta = 0.01$ at $Re = 1000$ and 1500. At $Re = 1000$, no transition has been detected for $\eta = 0.01$. As the Reynolds number increases to 1500, transition occurs after the energy of streaks reaches the maximum value. However, the transition cannot be sustained for long time. Comparing figure 20 with figure 19(*a*,*b*), it is shown that for fixed Re and ε, the energy of a disturbance is easier to sustain in the narrow-gap case than in the wide-gap case.

In order to show the characteristics of the structures of the flow field in the nonlinear stage after transition, we plot the disturbance flow field for $\eta = 0.1$ and 0.5 at $Re = 1500$ in figures 21 and 22. It can be observed that slow-speed streaks occupy the region near the inner cylinder, whereas fast-speed streaks are located near the outer cylinder. The structure in figures 21 and 22 is qualitatively similar to the exact coherent structures in SCF (Deguchi & Nagata 2011). Comparing figures 21 and 22 with figure 14, we find that the structure of the flow field in the nonlinear stage is significantly different from the structure of the optimal disturbance in which slow-speed and fast-speed streaks alternate in the spanwise direction.

7. Summary and conclusions

In the present paper the linear stability and nonlinear evolution in sliding Couette flow have been investigated using the energy method, the non-modal stability theory and direct numerical simulations.

We investigated the condition with no energy growth for both axisymmetric and non-axisymmetric disturbances. In the results of the eigenvalue analysis, instability only occurs in the case of $\eta \leqslant 0.1415$ and the stability of the flow is determined by axisymmetric perturbations. However, our results of the energy stability analysis

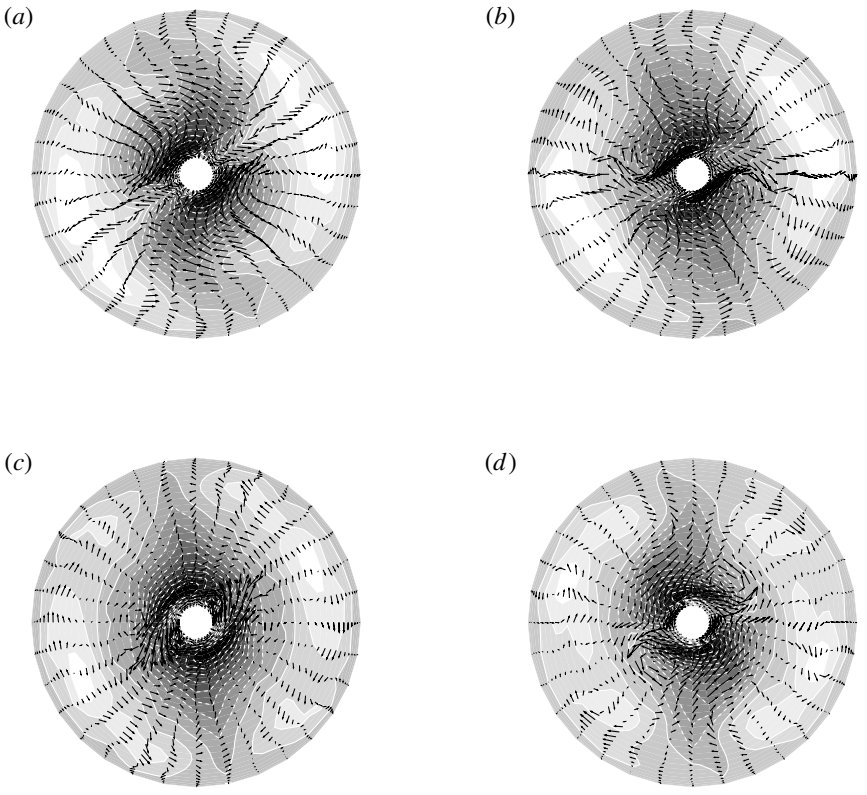

FIGURE 21. The disturbance flow field at $t = 400$ for $\eta = 0.1$, $n = 2$ and $Re = 1500$. The streamwise wavenumber $\alpha = 1$, and the amplitude of initial optimal streamwise vortices $\varepsilon = 0.05$. The arrows indicate the projection of the velocity on the cross-section $z = (k/4)(2\pi/\alpha)$, $k = 0, 1, 2, 3$ for (*a–d*) respectively. Grey scale represents the axial velocity component (light: fast, dark: slow). Positive and negative disturbance axial velocity components are denoted by the solid and the dashed lines.

are significantly different from those of the eigenvalue analysis. The results show that for all values of η, each mode of n can experience an energy growth at the initial time. In the wide-gap limit of $\eta \to 0$, the critical condition is determined by the non-axisymmetric disturbance with $n = 1$. For all values of η, the most unstable disturbance is in the form of streamwise-independent streaks. With the decrease of η, the azimuthal wavenumber of the most unstable mode increases. The azimuthal wavenumber of the most unstable mode can be estimated by $n \simeq 1.6(1 + \eta)/(1 - \eta)$.

The main focus of the present paper is the non-modal stability of sliding Couette flow. We study the response to external excitations and initial conditions. The response to external excitations is characterized using the ϵ-pseudospectrum, and the response to initial conditions is described by the energy growth function $G(t)$. For each value of η, both the axisymmetric and non-axisymmetric external forcing can be amplified by a rather large factor. However, the amplification of response to the axisymmetric external forcing is much lower than that to the non-axisymmetric one. Results show that the most amplified disturbance is achieved by streamwise-independent forcing at $\omega = 0$. With the increase of the frequency, the amplitude of the response to streamwise-independent external forcing decreases significantly. For each mode n, the maximum

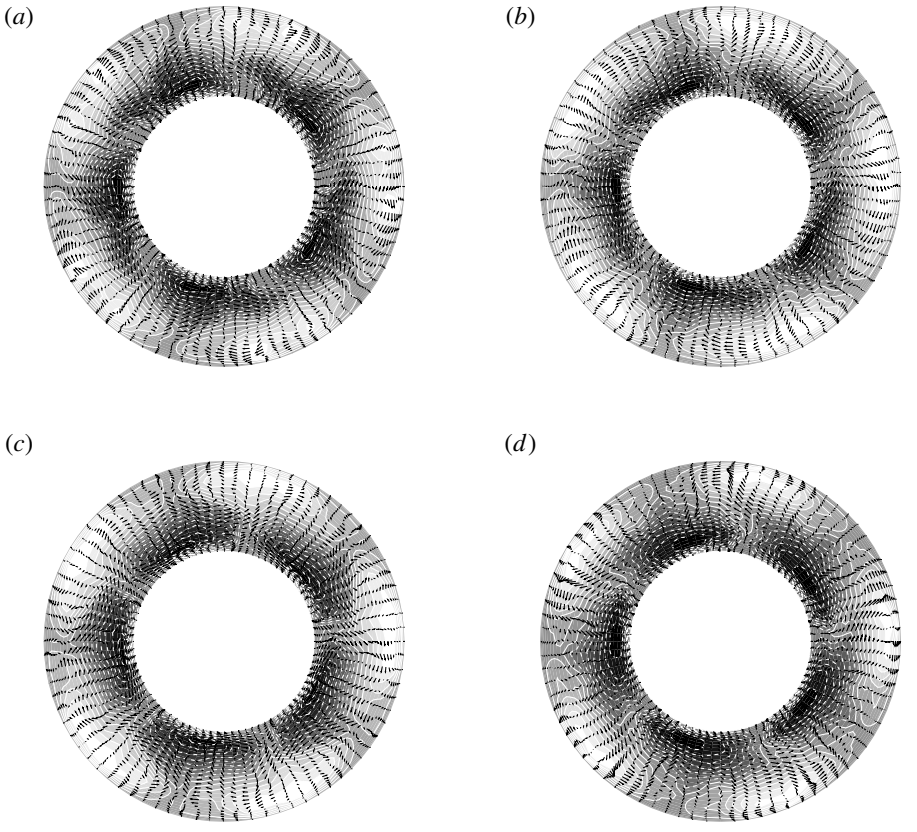

FIGURE 22. As figure 21 but for $\eta = 0.5$, $n = 5$.

response is realized at $\alpha = 0$. The streamwise wavenumber corresponding to the most amplified response increases with the increase of frequency. These results show that the streaks have the potential to be substantially amplified by external forcing through the lift-up effect.

We have also studied the transient energy growth of initial conditions. The results show that even if the Reynolds number is lower than the critical value predicted by linear stability analysis, the disturbance can be amplified substantially. For axisymmetric disturbances, the two-dimensional Reynolds stress mechanism is responsible for the transient energy growth. At the initial time, the flow pattern of the isolines of the streamfunction tilts opposite to the mean flow and the disturbance gains energy from the mean shear. At the optimal time, the flow pattern becomes upright and the disturbance neither gains energy from nor returns energy to the mean shear. After the optimal time, the flow pattern tilts towards the mean flow and returns energy to the mean flow. For non-axisymmetric disturbances, both the lift-up mechanism and the two-dimensional Reynolds stress are responsible for the transient energy growth. For all values of η, the most amplified disturbance is in the non-axisymmetric form. We studied the transient energy growth of various streamwise wavenumbers for a wide range of the Reynolds number. At low Reynolds numbers, for each $n \neq 0$ the maximum transient energy growth is realized at a non-zero streamwise wavenumber. In this case, the optimal response is in the form of helical streaks. This result is

different from that of pipe and plane Poiseuille flows in which the optimal response is in the form of straight streaks. With the increase of the Reynolds number, for each $n \neq 0$ the streamwise wavenumber of the most amplified disturbance decreases and tends to zero. This means that with the increase of the Reynolds number, the optimal response changes from a helical streak to a straight streak. We also studied the dependence of maximum energy growth on the Reynolds number. It is found that the maximum transient energy growth is of the order of Re^2 and the optimal time is of the order of Re. This relationship is qualitatively similar to the case of plane Couette flow, plane Poiseuille flow and pipe Poiseuille flow (Schmid & Henningson 2001). In our results, as η increases from 0.01 to 0.98, the maximum energy growth increases from $1.06\times10^{-4}Re^2$ to $2.90\times10^{-4}Re^2$. The latter is very close to the result for plane Couette flow. We studied the possible structures of optimal disturbances and found that the optimal response to initial conditions can be in three forms: streamwise-independent straight streaks, helical streaks and streamwise-dependent straight streaks.

Direct numerical simulations are applied to investigate the scenario of transition based on the transient growth of the optimal streamwise vortices and subsequent secondary instability of the modified base flow. The transient mechanism and nonlinear modification are responsible for the formation of the streaks. We perform a nonlinear simulation of the evolution of streamwise vortices with initial amplitude of ε. For small ε, the amplification of the energy of disturbances follows that of the linear case. With the increase of ε, both the maximum growth of energy and the maximum growth time decrease. For fixed Re and ε, the maximum growth of energy is lower in the wide-gap case than in the narrow-gap case. We studied the streak breakdown phase in the SV scenario by examining the instability of streamwise streaks. At fixed Re and η, the growth rate of the noise for breakdown increases with the amplitude of streamwise vortices. For $\varepsilon = 0.01$, streak instability occurs in the case of $\eta = 0.01$ at $Re = 1000$. However, $\varepsilon = 0.01$ is not sufficient to trigger streak instability in narrower-gap cases of $\eta = 0.1$ and 0.5. This means that even though the potential of streamwise vortices in the wide-gap case is lower than in the narrower-gap cases, the streak is more unstable in the wide-gap case for fixed Re and ε. The time evolution of the energy of the streamwise vortices with $\varepsilon = 0.05$ is examined for various η at $Re = 1000$ and 1500. For $\eta = 0.1$ and 0.5, the energy of disturbance is damped at $Re = 1000$. As the Reynolds number increases to $Re = 1500$, the energy of disturbance can be sustained. For the wide-gap case of $\eta = 0.01$, even for $Re = 1500$ the energy of disturbance gradually decays.

Acknowledgements

This work was supported by National Natural Science Foundation of China (Grants No. 11102211, No. 50890182, and No. 11072249) and the Knowledge Innovation Program of Chinese Academy of Sciences (KGCX-SW-409).

REFERENCES

ARNEY, M. S., BAI, R., GUEVARA, E., JOSEPH, D. D. & LIU, K. 1993 Friction factor and holdup studies for lubricated pipelining. I. Experiments and correlations. *Intl J. Multiphase Flow* **19**, 1061–1076.

BOTTARO, A., CORBETT, P. & LUCHINI, P. 2003 The effect of base flow variation on flow stability. *J. Fluid Mech.* **476**, 293–302.

BURRIDGE, D. M. & DRAZIN, P. G. 1969 Comments on 'stability of pipe Poiseuille flow'. *Phys. Fluids* **12**, 264–265.

BUTLER, K. M. & FARRELL, B. F. 1992 Three-dimensional optimal perturbations in viscous shear flow. *Phys. Fluids* A **4**, 1637–1650.

CANUTO, C., HUSSAINI, M. Y., QUARTERONI, A. & ZANG, T. A. 1993 *Spectral Methods in Fluid Dynamics*. Springer.

CHERUBINI, C., ROBINET, J. C., BOTTARO, A. & DE PALMA, P. 2010 Optimal wave packets in a boundary layer and initial phases of a turbulent spot. *J. Fluid Mech.* **656**, 231–259.

CHOMAZ, J. M. 2005 Global instabilities in spatially developing flows: non-normality and nonlinearity. *Annu. Rev. Fluid Mech.* **37**, 357–392.

DEGUCHI, K. & NAGATA, M. 2011 Bifurcation and instabilities in sliding Couette flow. *J. Fluid Mech.* **675**, 1–23.

ELLINGSEN, T. & PALM, E. 1975 Stability of linear flow. *Phys. Fluids* **18**, 487–488.

FAISST, H. & ECKHARDT, B. 2000 Transition from the Couette–Taylor system to the plane Couette system. *Phys. Rev.* E **61**, 7227–7230.

FAISST, H. & ECKHARDT, B. 2003 Travelling waves in pipe flow. *Phys. Rev. Lett.* **91**, 224502.

FARREL, B. F. & IOANNOU, P. J. 1993 Optimal excitation of three-dimensional perturbations in viscous constant shear flow. *Phys. Fluids* A **6**, 1390–1400.

FREI, C., LÜSCHER, P. & WINTERMANTEL, E. 2000 Thread-annular flow in vertical pipes. *J. Fluid Mech.* **410**, 185–210.

GITTLER, P. 1993 Stability of Poiseuille–Couette flow between concentric cylinears. *Acta Mechanica* **101**, 1–13.

HAMILTON, J. M., KIM, J. & WALEFFE, F. 1995 Regeneration mechanisms of near-wall turbulence structures. *J. Fluid Mech.* **287**, 317–348.

HUNG, W. L., JOSEPH, D. D. & MUNSON, B. R. 1972 Global stability of spiral flow. Part 2. *J. Fluid Mech.* **51**, 593–621.

JOSEPH, D. D. & MUNSON, B. R. 1970 Global stability of spiral flow. *J. Fluid Mech.* **43**, 545–575.

KITOH, O., NAKABYASHI, K. & NISHIMURA, F. 2005 Experimental study on mean velocity and turbulence characteristics of plane Couette flow: low-Reynolds-number effects and large longitudinal vortical structure. *J. Fluid Mech.* **539**, 199–227.

KLINE, S. J., REYNOLDS, W. C., SCHRAUB, F. A. & RUNSTADLER, P. W. 1967 The structure of turbulent boundary layers. *J. Fluid Mech.* **30**, 741–773.

LANDAHL, M. T. 1975 Wave breakdown and turbulence. *SIAM J. Appl. Maths* **28**, 735–756.

LANDAHL, M. T. 1980 A note on an algebraic instability of inviscid parallel shear flows. *J. Fluid Mech.* **98**, 243–251.

LIU, R. & LIU, Q. S. 2011 Non-modal instability in plane Couette flow of a power-law fluid. *J. Fluid Mech.* **676**, 145–171.

MALERUD, S., MÅLØY, K. J. & GOLDBURG, W. I. 1995 Measurements of turbulent velocity fluctuations in a planar Couette cell. *Phys. Fluids* **7**, 1949–1955.

NAGATA, M. 1990 Three-dimensional finite-amplitude solutions in plane Couette flow: bifurcation from infinity. *J. Fluid Mech.* **217**, 519–527.

ORR, W. M. F. 1907 The stability or instability of the steady motions of a perfect liquid and of a viscous liquid. *Proc. R. Irish Acad.* A **27**, 9–138.

ORSZAG, S. A. & KELLS, L. C. 1980 Transition to turbulence in plane Poiseuille and plane Couette flow. *J. Fluid Mech.* **96**, 159–205.

ORSZAG, S. A. & PATERA, A. T. 1983 Secondary instability of wall-bounded shear flows. *J. Fluid Mech.* **128**, 347–385.

PEDLOSKY, J. 1987 *Geophysical Fluid Dynamics*, 2nd edn. Springer.

PREZIOSI, L. & ROSSO, F. 1990 Stability of a viscous liquid between sliding pipes. *Phys. Fluids* A **2** (7), 1158–1162.

REDDY, S. & HENNINGSON, D. S. 1993 Energy growth in viscous channel flows. *J. Fluid Mech.* **252**, 209–238.

REDDY, S. C., SCHMID, P. J., BAGGETT, J. S. & HENNINGSON, D. S. 1998 On stability of streamwise streaks and transition thresholds in plane channel flows. *J. Fluid Mech.* **365**, 269–303.

SCHMID, P. J. 2007 Nonmodal stability theory. *Annu. Rev. Fluid Mech.* **39**, 129–162.

SCHMID, P. J. & HENNINGSON, D. S. 1994 Optimal energy density growth in Hagen–Poiseuille flow. *J. Fluid Mech.* **277**, 197–225.

SCHMID, P. J. & HENNINGSON, D. S. 2001 *Stability and Transition in Shear Flows*. Springer.

TILLMARK, N. & ALFREDSSON, P. H. 1992 Experiments on transition in plane Couette flow. *J. Fluid Mech.* **235**, 89–102.

TREFETHEN, L. N. & EMBREE, M. 2005 *Spectra and Pseudospectra: The Behavior of Non-normal Matrices and Operators*. Princeton University Press.

TREFETHEN, L. N., TREFETHEN, A. E., REDDY, S. C. & DRISCOLL, T. A. 1993 Hydrodynamics stability without eigenvalues. *Science* **261**, 578–584.

WALEFFE, F. 1995 Hydrodynamic stability and turbulence: beyond transients to a self-sustaining process. *Stud. Appl. Maths* **95**, 319–343.

WALEFFE, F. 1997 On a self-sustaining process in shear flows. *Phys. Fluids* **9** (4), 883–900.

WALTON, A. G. 2003 The nonlinear instability of thread–annular flow at high Reynolds number. *J. Fluid Mech.* **477**, 227–257.

WALTON, A. G. 2004 Stability of circular Poiseuille–Couette flow to axisymmetric disturbances. *J. Fluid Mech.* **500**, 169–210.

WALTON, A. G. 2005 The linear and nonlinear stability of thread-annular flow. *Phil. Trans. R. Soc. Lond.* A **363**, 1223–1233.

WEDIN, H. & KERSWELL, R. R. 2004 Exact coherent structures in pipe flow: travelling wave solutions. *J Fluid Mech.* **508**, 333–371.

WYGNANSKI, I. & CHAMPAGNE, F. 1973 On transition in a pipe. Part 1. The origin of puffs and slugs and the flow in a turbulent slug. *J Fluid Mech.* **59**, 281–335.

WYGNANSKI, I., SOKOLOV, M. & FRIEDMAN, D. 1975 On transition in a pipe. Part 2. The equilibrium puff. *J Fluid Mech.* **69**, 283–304.